

Competing Orbital Magnetism and Superconductivity in electrostatically defined Josephson Junctions of Alternating Twisted Trilayer Graphene

Vishal Bhardwaj^{1†}, Lekshmi Rajagopal^{1†}, Lorenzo Arici¹, Matan Bocarsly¹, Alexey Ilin¹, Gal Shavit⁵, Kenji Watanabe³, Takashi Taniguchi⁴, Yuval Oreg¹, Tobias Holder⁶, Yuval Ronen^{1*}

Abstract:

The coexistence of superconductivity and magnetism within a single material system represents a long-standing goal in condensed matter physics. Van der Waals-based moiré superlattices provide an exceptional platform for exploring competing and coexisting broken symmetry states. Alternating twisted trilayer graphene (TTG) exhibits robust superconductivity at the magic angle of 1.57° and 1.3° , with suppression at intermediate twist angles. In this study, we investigate the intermediate regime and uncover evidence of orbital magnetism. As previously reported, superconductivity is suppressed near the charge neutrality point (CNP) and emerges at larger moiré fillings. Conversely, we find orbital magnetism most substantial near the CNP, diminishing as superconductivity develops. This complementary behavior is similarly observed in the displacement field phase space, highlighting a competitive interplay between the two phases. Utilizing gate-defined Josephson junctions, we probe orbital magnetism by electrostatically tuning the weak links into the magnetic phase, revealing an asymmetric Fraunhofer interference pattern. The estimated orbital ferromagnetic ordering temperature is approximately half the superconducting critical temperature, coinciding with the onset of Fraunhofer asymmetry. Our findings suggest that the observed orbital magnetism is driven by valley polarization and is distinct from the anomalous Hall effect reported at integer fillings in twisted graphene systems. These results offer insights into the interplay between superconductivity and magnetism in moiré superlattices.

¹Department of Condensed Matter Physics, Weizmann Institute of Science, Rehovot 7610001, Israel

³Research Center for Functional Materials, National Institute for Materials Science, Tsukuba 305-0044, Japan

⁴International Center for Materials Nanoarchitectonics, National Institute for Materials Science, Tsukuba 305-0044, Japan

⁵Department of Physics and Institute for Quantum Information and Matter, California Institute of Technology, Pasadena, California 91125, USA

⁶School of Physics and Astronomy, Tel Aviv University, Tel Aviv 69978, Israel

[†]These authors contributed equally to this work

*yuval.ronen@weizmann.ac.il

Exploring exotic phases arising from strong electron-electron interactions has captivated the condensed matter physics community, unveiling a variety of correlated phases such as superconductivity, magnetism, and topological states^{1,2}. Flat energy bands, where the kinetic energy is suppressed, have emerged as a fertile ground for these phases, as the dominance of interaction energy facilitates the emergence of correlated phenomena³⁻⁵. Twisted van der Waals (vdW) heterostructures, with their tunable moiré superlattices, have led to groundbreaking discoveries, including superconductivity⁶⁻⁸, orbital magnetism^{9,10}, Chern insulators^{11,12}, and, more recently, zero magnetic field fractionally correlated insulators¹³. Among these phenomena, orbital magnetism in twisted graphene systems stands out due to its potential to coexist with superconductivity, opening avenues for realizing non-abelian anyons in hybrid systems—a highly sought-after goal in condensed matter physics¹⁴. However, understanding the interplay between these two phases remains a significant challenge.

Twisted bilayer graphene (TBG) at the ‘magic angle’ of $\sim 1.1^\circ$ was the first system to demonstrate flat bands and correlated insulating and superconducting phases^{6,15,16}. The twist angle between the atomically thin layers creates a moiré superlattice, where electrons can become asymptotically localized. This localization results from the fine-tuned destructive interference of wavefunction overlaps at the atomic scale, leading to a minimal net kinetic energy. Introducing a third graphene layer, with the top and bottom layers mirror-symmetric relative to the middle layer ($\theta_{TM} = -\theta_{MB} = 1.57^\circ$), creates a moiré superlattice with a periodicity of approximately 9 nm. At this angle, the twisted trilayer graphene (TTG) band structure develops flat bands and an additional gapless Dirac cone characteristic of monolayer graphene (MLG)^{7,17}. TTG offers a tunable platform to study superconductivity, which depends on density and displacement field. It has shown robust superconductivity compared to TBG, persisting over a wide range of twist angles from 1.57° to approximately 1.2° , and enduring magnetic fields that violate the Pauli limit^{18,19}, hinting towards an unconventional nature. Surprisingly, superconductivity is suppressed at intermediate twist angles around 1.4° ^{19,20}.

Meanwhile, orbital magnetism has been observed in graphene-based heterostructures with broken inversion symmetry due to alignment with hexagonal boron nitride (hBN)²¹⁻²³ and in off-magic-angle unaligned TBG²⁴. However, these systems typically lack the coexistence of superconductivity and orbital magnetism, as time-reversal symmetry breaking, required for magnetism, tends to destabilize superconducting phases. Theoretically, superconductivity and orbital magnetism can emerge in flat-band systems driven by strong interactions. The coexistence of these phases has been reported in TBG, where superconductivity accompanies anomalous Hall effect at a moiré filling factor of $\nu = 1$ ²⁵. Yet, the competition and coexistence of these phases remain poorly understood in TTG, particularly in intermediate twist angles.

In this work, we report the competition of superconductivity and OM in alternating TTG heterostructures with three previously unexplored twist angles of 1.38° , 1.41° and 1.44° . We observe OM through sharp slope changes (jumps) in the Hall resistance around zero out-of-plane magnetic fields near the charge neutrality point in both electron and hole doping regions, accompanied by weak hysteresis. OM persists up to moiré densities or displacement fields where superconductivity emerges; see Fig. 1a for a schematic phase diagram of OM and superconductivity in TTG as a function of twist angle, θ , moiré filling factor, ν , and displacement field, D . We employed an electrostatically defined Josephson junction to probe the nature of the weak link, tuning it between different phases. When the weak link is tuned to the OM phase, we observe an asymmetric Fraunhofer pattern, likely caused by current-induced magnetization switching. The ordering temperature of the magnetic phase is estimated to be ~ 650 mK, less than the critical temperature for superconductivity (1.3K). These observations suggest that, in this twist angle range, TTG exhibits key differences in its phase diagram compared to twisted bilayer graphene (TBG), with a distinct interplay between superconducting and magnetic phases.

Our vdW heterostructures consist of alternating TTG layers, with the bottom and top graphene layers twisted mirror-symmetrically relative to the middle layer. The TTG heterostructure is encapsulated by top and bottom insulating hBN layers with a 25 nm and 30 nm thickness, respectively, and placed on top of a Si/SiO₂ substrate serving as a back gate. We fabricate the heterostructure into three consecutively connected Hall bars, A, B, and C, by introducing a Ti/Au top gate. We make use of the variation in the angle along the TTG heterostructure to study the OM (Fig. 1b) and make use of the linked regions between A-B (200 nm) and B-C (100 nm) to form Josephson junctions to study supercurrent flow-mediated *via* the OM region (Fig. 1b). For additional information on the heterostructure and device fabrication, see supplementary information (SI) section 1 and Fig. S1.

The carrier density, n , and displacement field, D , in the TTG are electrostatically tuned by both top and bottom gate voltages (V_{BG} , V_{TG}) coupled by their respective capacitances (C_{BG} , C_{TG}), see SI section 1. The device transport properties were measured in a dilution refrigerator with a base temperature of 10 mK equipped with a 9-1-1 T vector magnet using a standard low-frequency lock-in technique; see methods section and SI section 1. The twist angles (θ) of the devices are estimated by measuring the moiré superlattice carrier density $n_s = 8\theta^2 / \sqrt{3} a^2$ ($a=0.23\text{nm}$) and are found to be 1.38°, 1.41°, and 1.44° for A, B, and C, respectively; see SI section 1. The 4-terminal longitudinal (R_{xx}) and transverse (R_{xy}) resistance as a function of carrier density and magnetic field at zero displacement field, D , for devices A, B, and C, are shown in extended Fig 1. The R_{xx} (R_{xy}) for devices A, B, and C are measured across the contacts configuration shown in Fig. 1b; see SI section 1 for more information. Similar to previous reports on TTG, we observe Chern Insulator (CI) states, giving rise to peaks of resistance screened by the Dirac spectrum of MLG at a moiré filling factor, ν , of $\nu = 1, 2, 3, 4, -2, -4$ in all devices. Robust superconductivity pockets on both electron and hole-doped regions, with a maximum critical temperature of $T_{SC} \sim 1.3$ K (electron-doped at $\nu \sim 2.6$ and $D \sim 0.38\text{V/nm}$) are observed in device C and across the Josephson junction of devices B and C (see extended Fig 3 and supplementary Fig. S6(a)).

By examining the variation of R_{xy} as a function of the out-of-plane magnetic field, B_z , we mapped out the linear Hall dependence as a function of the filling factor. However, unexpectedly, at certain filling factors near the charge neutrality point (CNP), a sudden increase in the slope develops (at $B_z=0$), as highlighted by the purple line in Fig. 1c, measured at $\nu = -0.45$ and $D = 0\text{ V/nm}$. As the filling factor or displacement field increased, the slope reverts to its expected linear behavior. To further explore the phase space where the increased slopes in R_{xy} occur as a function of the filling factor and displacement field, we measured R_{xy} as a function B_z and ν at $D = 0\text{ V/nm}$ and $D = 0.6\text{ V/nm}$. The Landau-level fan diagrams of $\frac{dR_{xy}}{dB_z}$ for device A, as a function of ν at $D = 0\text{ V/nm}$ and $D = 0.6\text{ V/nm}$ are shown in Fig. 1d and 1e, respectively. These plots of $\frac{dR_{xy}}{dB_z}$ highlight the regions with increased slopes by the darker color regions around $B_z=0$. In Fig. 1d, as ν increases away from CNP, the diminishing intensity of the darker regions becomes evident, indicating the suppression of the jumps in R_{xy} . At high displacement field $D = 0.6\text{ V/nm}$ the R_{xy} jumps in the vicinity of CNP likewise decrease, as seen in Fig. 1e; see also the blue line cut at $\nu = -0.45$ in Fig. 1c. The resistive peaks at $\nu = 1, 3, -3$ are also no longer observed. Finally, the $\frac{dR_{xy}}{dB_z}$ slope extracted after subtracting the linear Hall effect is shown in the inset of extended Fig. 2 as a function of ν for all three Hall bar devices. The maximum slope is observed on the hole doping side around $\nu = -0.45$, and the jumps in R_{xy} disappear for $\nu > 2$ and $\nu < -2$, see black line cut in Fig. 1c at $\nu = -3.6$ and $D = 0\text{ V/nm}$. We observed a slight hysteresis behavior (see Figure S4 of SI), likely due to the presence of multiple magnetic domains.

In Fig. 1f and 1g, we extract the Hall carrier density, $n_H = 1/e * \frac{dR_{xy}}{dB_z}$, as a function of the filling factor, ν at $B_z=0$, see SI section 2 and Fig. S2 for more information. Fig. 1f shows n_H vs. ν plot at $D = 0 \text{ V/nm}$, where we observe resets at integer $\nu = 1, \pm 2, \pm 3, \pm 4$, indicative of Chern insulator states at these integer fillings^{17,26}. However, instead of a linear slope in n_H vs. ν , an offset is observed from both doping regions of the CNP, emanating from fractional fillings of $\nu \sim -0.5$ and 0.7 , see SI section 1 and Fig. S2(a) for more information. This abrupt change in DOS hints towards an intrinsic effective magnetic field, which might originate from spontaneous symmetry breaking of degenerate bands near the CNP^{27,28}. We repeated the analysis at $D = 0.6 \text{ V/nm}$, in Fig. 1g, where the expected linear Hall magnetic field dependence was restored around CNP.

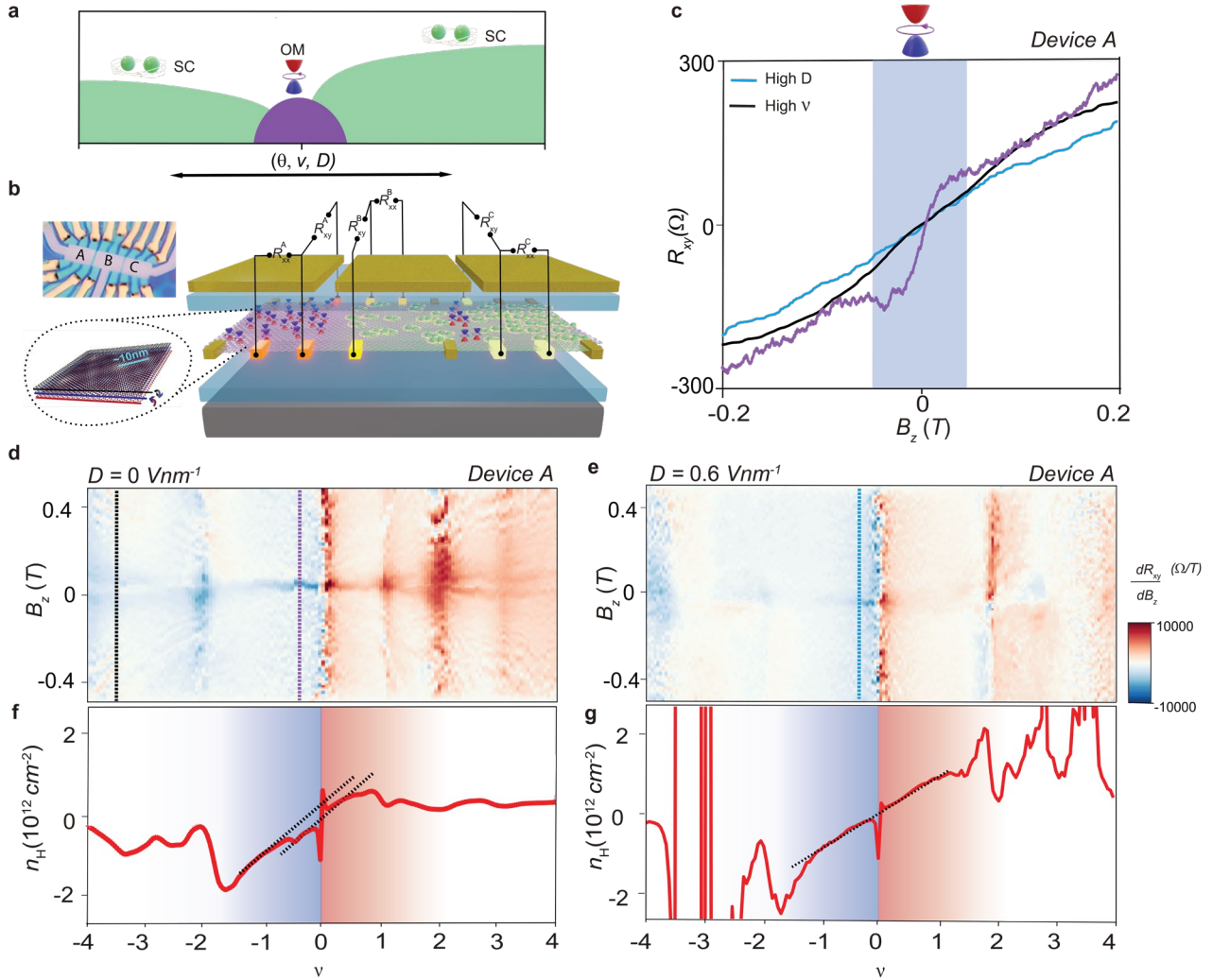


Figure 1: Density tunable jumps in Hall measurements. (a) Schematic phase space of superconductivity and orbital magnetism in alternating TTG as a function of twist angle θ moiré filling factor ν and displacement field D . (b) Schematic diagram of alternating TTG Hall bar devices and in situ gate defined Josephson junctions between them. The TTG is encapsulated by hBNs on both sides, metal (Au/Ti) gated on top and bottom gated using oxidized silicon (Si/SiO₂ 285nm). An enlarged picture of alternating TTG and an optical image of the device are shown alongside. The moiré length is extracted using the formula $\lambda = a/[2 \sin(\theta/2)]$ ($a = 0.246 \text{ nm}$ and $\theta=1.40^\circ$). (c) The line scans of R_{xy} as a function of B_z at three distinct (ν, D) values *i.e.* purple line at $\nu = -0.45$ and $D = 0 \text{ V/nm}$, black line at $\nu = -3.6$ and $D = 0 \text{ V/nm}$ (high ν), blue line at $\nu = -0.45$ and $D = 0.6 \text{ V/nm}$ (high D) for device A. Corresponding colors of line cuts are shown

in Fig. (d) and (e). **(d)** and **(e)** The Landau fan diagram of B_z v/s ν for differential Hall resistance w.r.t magnetic field ($\frac{dR_{xy}}{dB_z}$) at $D=0V/nm$ and $D=0.6 V/nm$ respectively for device A. **(f)** and **(g)** The variation of Hall carrier density (n_H) with ν at $B_z=0$ at $D=0V/nm$ and $D=0.6 V/nm$ respectively for device A.

The mirror-symmetric configuration of graphene layers in TTG enables the exploration of hybridization effects between the Dirac and flat band sectors using a displacement field. Figures 2a and 2b present the phase space of $\frac{dR_{xy}}{dB_z}$ as a function of B_z and D , at $\nu = -0.45$ and 0.7 , respectively for device A. Darker colors correspond to larger magnitudes of $|\frac{dR_{xy}}{dB_z}|$. In Fig. 2a, at $\nu = -0.45$, a jump in R_{xy} is observed at $D = 0 V/nm$ (indicated by the brown color), as also seen in Fig. 1c. This jump is suppressed as the displacement field increases beyond $|D| > 0.5 V/nm$. In Fig. 2b, at $\nu = 0.7$, an opposite slope in R_{xy} is observed, with jumps in R_{xy} (indicated by the blue color) being suppressed for $|D| > 0.25 V/nm$. These findings suggest that the displacement field in TTG enables a tunable hybridization between the monolayer Dirac sector and the flat bands sector, leading to the vanishing of OM.

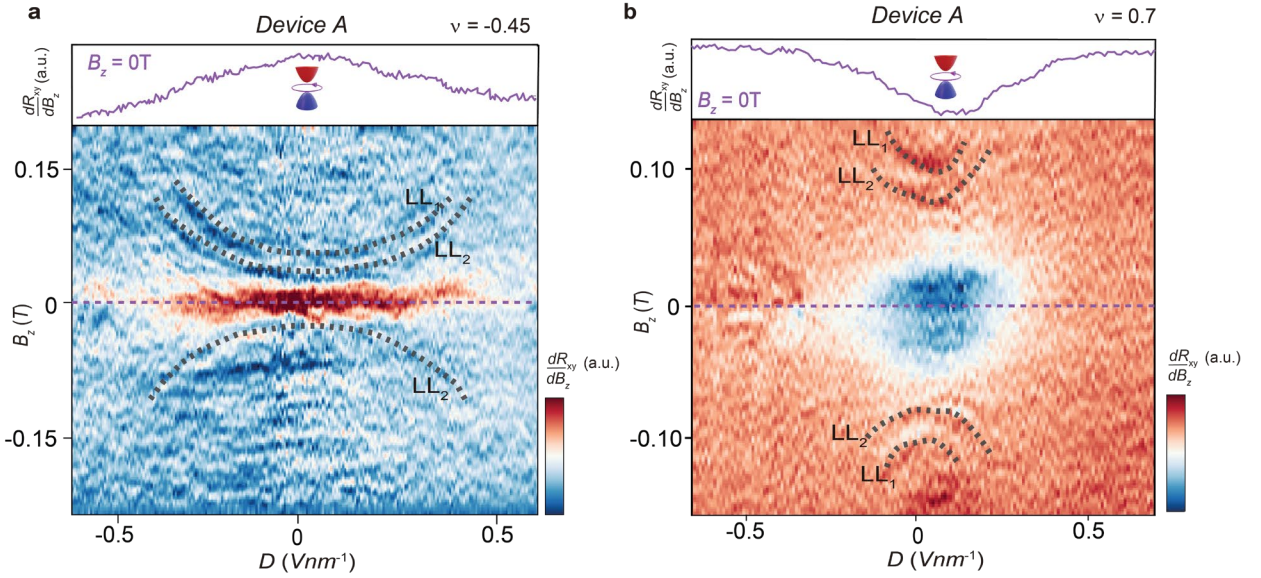


Figure 2: Displacement field tunable jumps in Hall measurements. The displacement field (D) dependence of $\frac{dR_{xy}}{dB_z}$ while sweeping B_z around $0T$ for device A. The moiré filling factor (ν) is fixed at **(a)** $\nu=-0.45$ and **(b)** $\nu=0.70$. The dark brown (Fig. a) and blue regions (Fig. b) nearby $B_z = 0T$ show the maximum change in $\frac{dR_{xy}}{dB_z}$, which disappear at high D . Insets show the line cuts at $B_z = 0T$, corresponding to purple dash lines in figures. The dotted curved black lines represent the variation of Landau levels 1 (LL_1) and 2 (LL_2) of the monolayer Dirac sector with D .

Band mixing is thought to play a crucial role in determining the nature of the correlated low-energy phases^{29,30}. To quantify the hybridization of the two sectors, we analyze the parabolic dashed curves highlighted in Fig. 2. These curves correspond to the Shubnikov-de Haas (SdH) oscillations of the MLG Landau levels (LL_s), at specific Fermi energies E_F for a constant ν ^{6,30,31}. By examining the shift in the MLG LL_s , we can infer the degree of hybridization between the two sectors. If we assume the Fermi velocity, $v_F = dE/dk$ of MLG Dirac cone is $10^6 m/s$ at $D=0V/nm$, we can estimate the percentage change in v_F with increase in D , see SI section 2 for more details. At $\nu = -0.1$, -0.45 and -0.70 for an increase in D from 0 to $0.20 V/nm$, v_F decreases by $\sim 30\%$, 20% and 12% respectively. The MLG LL curvature lines

disappear at $D \sim 0.45, 0.4$ and 0.25 V/nm at $\nu = -0.1, -0.45$ and -0.70 respectively, coinciding with the disappearance of OM, See Fig. 2a, 2b and S3a. Thus, we conclude nearby CNP, a higher value of D is required for the hybridization of MLG with the flat bands and OM persists over longer ranges of D . However, as we increase the density, a smaller value of D is sufficient for hybridization since the Fermi energy is closer to the overlap between MLG and flat bands³¹. In ref²⁹ singlet superconductivity is predicted to emerge near CNP at low displacement fields in TTG. The observation of OM near CNP in our samples might explain the absence of such a singlet superconducting state due to competing ordering tendencies.

Magnetic ordering is a result of exchange interactions due to time-reversal symmetry breaking and can be observed due to spin magnetic moments or electron circular motion-driven orbital magnetic moments. While spin magnetic moments are typically isotropic, orbital moments are highly anisotropic. Previous studies have indicated that magnetism in graphene-based heterostructures is predominantly of orbital origin^{19,21-24,32}. To determine the dominant mechanism behind the magnetic state, we measured R_{xy} while varying the angle between the magnetic field and the sample plane. Fig. 3a shows R_{xy} as a function of $\vec{B} = B\cos(\theta) \cdot \hat{z} + B\sin(\theta) \cdot \hat{x}$ at $\nu = -0.45$ and $D = 0$ V/nm for device A. The angle θ between the sample and \vec{B} is varied from 90° to 0° in the steps of 15° . The steepest slope in R_{xy} is observed when $\vec{B} = B_z \cdot \hat{z}$, while no jump is detected when $\vec{B} = B_x \cdot \hat{x}$, indicating the highly anisotropic nature of the magnetic state. See fig. S5 of SI for the same measurements on device C and D. The inset of Fig. 3a shows R_{xy} measured as a function of B_z while a fixed $B_x = 0, 0.5$ and 1 T is applied. The amplitude of the R_{xy} jump remains unchanged even with B_x applied up to 1 T. This high out-of-plane anisotropy of the magnetic moments makes an orbital origin highly likely.

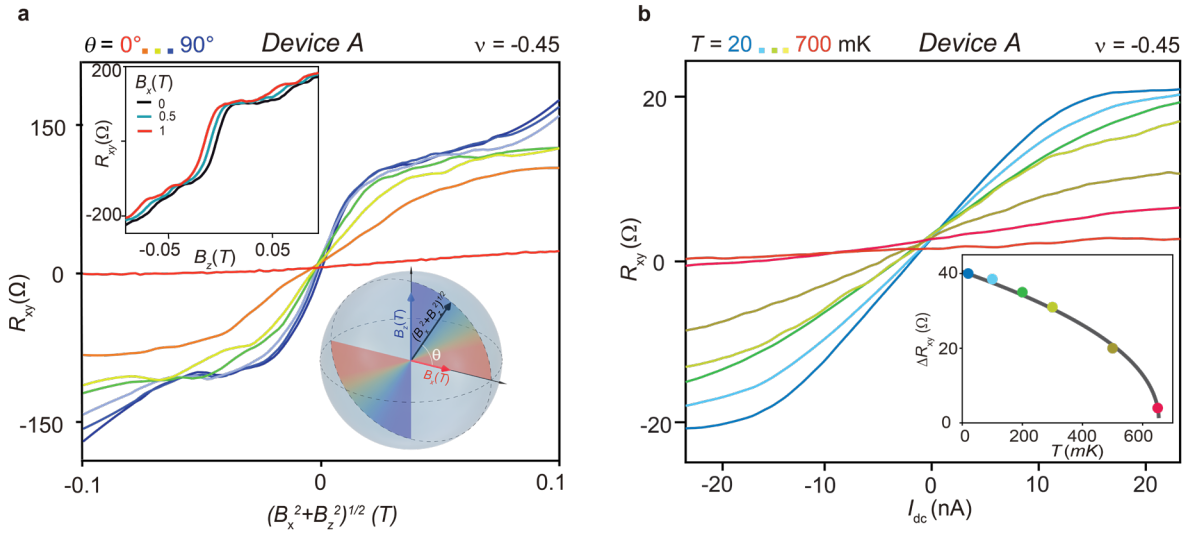


Figure 3: Confirming the orbital nature of the jumps in R_{xy} . (a) The R_{xy} vs $B = (B_x^2 + B_z^2)^{1/2}$ at varying θ between sample and B from 90° (blue) to 0° (red) in steps of 15° for device A. Inset shows the jumps in R_{xy} as a function of B_z at constant in-plane field $B_x = 0, 0.5$ and 1 T. (b) The temperature dependence of jumps in R_{xy} as a function of DC bias current (I_{dc}) at temperatures ranging from 20 mK (blue) to 700 mK (red) measured at $B_z = 0$ T for device A. Inset shows a fit of the jump height in R_{xy} (ΔR_{xy}) to the Curie Bloch equation: $\Delta R_{xy} = p(1 - T/T_{OM1})^\alpha$.

In studies on TBG aligned with hBN, orbital magnetic moments were polarized using an external DC bias (I_{dc}) superimposed on a small AC signal^{21,23}. We measured R_{xy} at $\nu = -0.45$ and $D = 0$ V/nm with an AC excitation of approximately 1 nA while varying the I_{dc} from -25 nA to $+25$ nA at $B_z = 0$ T. A jump in R_{xy} is observed at 20 mK, and the

amplitude of this jump decreases with increasing temperature. Fig. 3b shows the measurements taken up to 700 mK, with no jump observed above approximately 650 mK. The difference in R_{xy} at $I_{dc} = -20\text{nA}$ and $+20\text{nA}$ *i.e.* ΔR_{xy} can be fitted to the Curie Bloch equation $\Delta R_{xy} = p(1 - T/T_{OM1})^\alpha$ (here p is a proportionality constant, α is the fitting exponent and T_{OM1} is the critical temperature of the magnetic state) yielding $T_{OM1} = 654 \pm 6$ mK, $p = 40.5 \pm 1 \Omega$ and $\alpha = 0.45 \pm 0.05$.

The observed jumps in Hall resistivity as a function of bias current indicate the coupling between electric fields generated by currents in the conducting bulk and the magnetization of sample³³. Recent observations of I_{dc} induced switching of R_{xy} in TBG aligned to hBN are attributed to an interplay between extrinsic breaking of sublattice symmetry (due to alignment with hBN), breaking of rotation symmetries (due to strain), and intrinsic spontaneous time-reversal symmetry breaking³³. Rotation symmetry (C_3) breaking in TTG was recently reported *via* observation of transport non-reciprocity³⁴ and a nematic semimetal ground state at CNP³¹. Our results implicate the orbital magnetic moments, due to the spontaneous breaking of valley isospin symmetry near the CNP, as the culprits in facilitating the significant current-magnetization coupling. Indeed, TTG has shown evidence of exchange interactions for $\nu < 1.5$, while at higher densities, the charging self-energy becomes dominant³¹.

We now turn to investigate the impact of OM on supercurrent flow by incorporating it as the weak link in an electrostatically defined Josephson junction (JJ)^{35,36}, leveraging the tunable superconductivity in TTG. Valley polarization-driven OM resulted in asymmetric Fraunhofer patterns in previous graphene-based twisted devices^{19,32}. Extended Fig. 3a-c presents the R_{xx} measurements for all three devices under various displacement fields. As observed previously, superconductivity is enhanced at high displacement fields^{7,8} (in device C) and suppressed at twist angles between 1.38° and 1.41° , consistent with earlier studies^{19,37}. The phase space of R_{xx} due to the JJ weak link between devices B and C (JJ2 contacts 5-6 of JJ2, see supplementary Fig. S1) is shown in extended Fig. 4a. We observe clear resistive states and superconductivity across JJ (yellow dashed lines correspond to left and right-side ν in extended Fig. 4a). The vertical resistive lines in pink correspond to the filling factor (ν_j) of the weak link region with only the back gate applied.

Figures 4a, 4b, and 4c show the critical current as a function of out-of-plane magnetic field, B_z , for various phases of the weak link. The differential resistance (dV/dI) was measured at 20mK with an AC excitation of 1nA while sweeping the DC component of the current, I_{dc} . The left and right sides of JJ are tuned to a superconducting state (S) corresponding to $\nu \sim 2.6$ using a combination of top and bottom gates. The weak link is tuned to a superconducting state (S') $\nu_j \sim -2.7$ ($D_j \sim -0.3\text{V/nm}$), normal metallic state (N) $\nu_j \sim -1.7$ ($D_j \sim -0.19\text{V/nm}$) and orbital magnetic state (OM) $\nu_j \sim -0.45$ ($D_j \sim -0.05\text{V/nm}$) using the back gate only, as shown in the insets of Figs. 4a, 4b and 4c respectively. The line cuts of dV/dI vs I_{dc} at $B_z = 0\text{G}$ for these JJ configurations are shown in supplementary Fig S6 (b).

Fig. 4a presents a typical 2D measurement for the S|S|S configuration, where no Fraunhofer pattern is observed, confirming the presence of a relatively uniform superconducting region extending from the reservoirs across the weak link. As expected in this configuration, the maximum positive superconductivity critical current ($I_{c,max}^+$) and maximum negative superconductivity critical current ($I_{c,max}^-$) curves are symmetric along B_z axis, see inset of Fig.4a. In the S|N|S configuration, a supercurrent is observed across the JJ, exhibiting Fraunhofer oscillations as a function of B_z (Fig. 4b). The high-field periodicity of these oscillations, for a 2D superconductor, is predicted to follow $\Delta B \sim 1.8\Phi_0/w^2$, where Φ_0 is the flux quantum and w the lateral width of the JJ³⁸, which for our device evaluates to $\Delta B \sim 10\text{G}$. We observe B_z -induced oscillations with a width of $\sim 30\text{G}$ for the central maxima and a periodicity of $\sim 10\text{G}$ for the high-field oscillations. The Fraunhofer pattern also shows symmetric $I_{c,max}^+$ and $I_{c,max}^-$, as seen in the inset of Fig. 4b. Remarkably, as we move to the S|OM|S configuration, we observe asymmetric $I_{c,max}^+$ and $I_{c,max}^-$ along the B_z axis, (Fig. 4c). The asymmetry of the

Fraunhofer pattern decreases with an increase in temperature, as shown in the extended Fig. 4b, and a symmetric pattern is obtained at $\sim 650\text{mK}$.

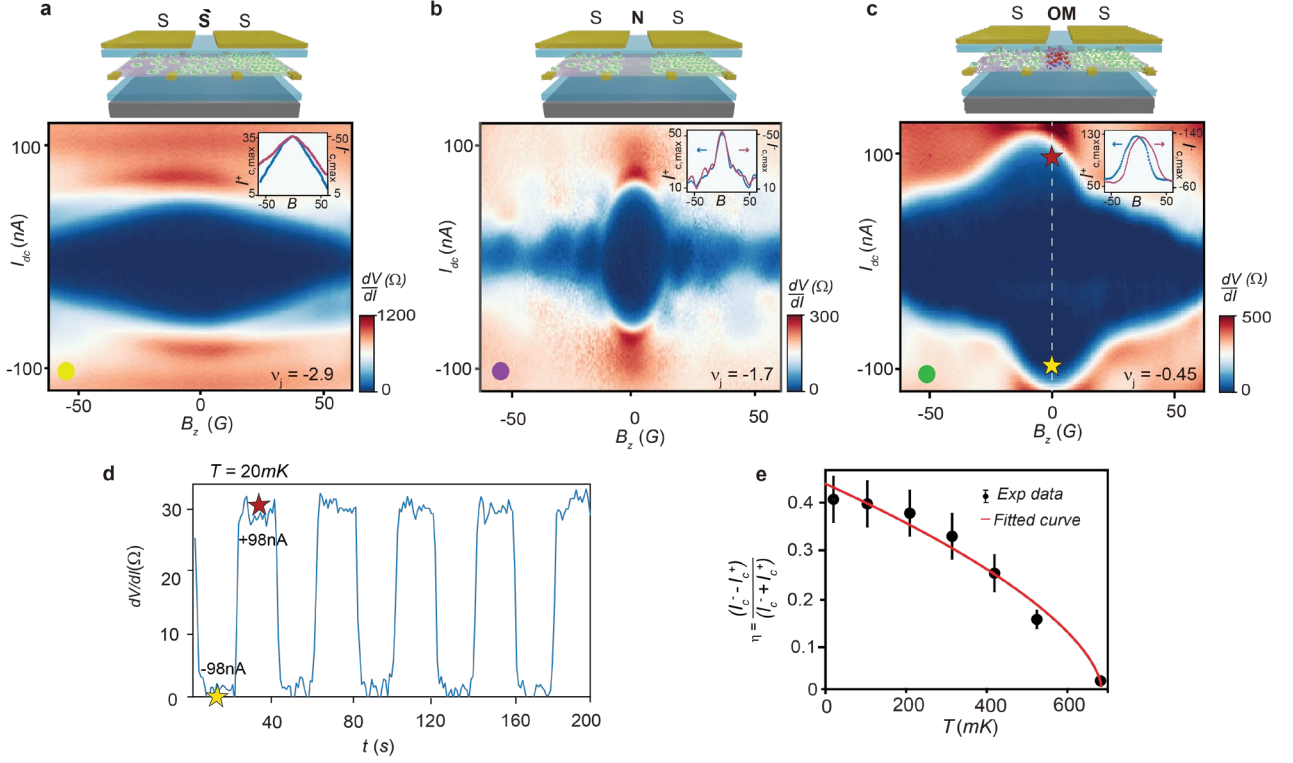


Figure 4: Gate defined Josephson junction as a probe for orbital magnetism. The Fraunhofer patterns measurements across JJ2 (contacts 5-6, see SI Fig. S1), left and right side of JJ tuned to superconducting state (S) at $\nu \sim 2.6$ and weak link tuned to (a) $\nu_j \sim -2.7$ forming S|S'|S JJ, (b) $\nu_j \sim -1.7$ forming S|N|S JJ and (c) $\nu_j \sim -0.45$ forming S|OM|S JJ. Insets on top of the figures show the schematics corresponding to JJ configurations. Top right insets show the line cuts of the positive SC critical current ($I_{c,max}^+$) and negative SC critical current ($I_{c,max}^-$) extracted from corresponding Fraunhofer patterns. (d) The dV/dI (Ω) characteristics of S|OM|S JJ measured at $B_z=0$ G while alternating I_{dc} between I_c^- (-98nA) and $-I_c^-$ (+98nA) after every 20 seconds at 20mK. (e) The measure of asymmetry in critical currents $\eta = \frac{(I_c^- - I_c^+)}{(I_c^- + I_c^+)}$ is plotted as a function of temperature (black data points) at $B_z=0$ G. The red line corresponds to fit the Curie Bloch equation $\eta = k(1 - T/T_{OM2})^\beta$.

We switch from the superconducting (SC) to the normal state at $B_z=0$, by alternating I_{dc} from 98nA to -98nA, respectively, illustrated by white dashed line in Fig. 4c. Fig. 4d shows the dV/dI characteristics, at 20mK, plotted over time. The resistance across the JJ switched between 0Ω (SC state) and $29 \pm 4 \Omega$ (normal) following the SC diode effect, disappearing at 650mK (see SI Fig. S7a). In Fig. 4e, we quantify the asymmetry of the Fraunhofer pattern by calculating $\eta = \frac{(I_c^- - I_c^+)}{(I_c^- + I_c^+)}$, where I_c^- and I_c^+ are the critical currents measured across for various temperatures (see SI Fig. S6c). As the temperature increases, η gradually decreases, reaching zero at 650mK, where the Fraunhofer pattern becomes symmetric, see extended Figs. 4(b-c) for additional details. By fitting η to the Curie Bloch equation, $\eta = k(1 - T/T_{OM2})^\beta$, where k is a proportionality constant, T is the temperature, and T_{OM2} the critical temperature, we obtained the following parameters: $k=0.44 \pm 0.06$, $\beta \sim 0.6 \pm 0.2$, and $T_{OM2} \sim 650 \pm 20\text{mK}$.

The estimated values of T_{OM2} matches well with the temperature estimated from R_{xy} vs. I_{dc} fits in Fig. 3b. This indicates that the asymmetry in the Fraunhofer pattern observed in the S|OM|S configuration is related to orbital

magnetism and possibly magnetic domain boundaries motion. We also note that other configurations, Figs. a-b, are symmetric, ruling out the possibility of an intrinsic device-related phenomenon^{32,39}.

We observed OM in TTG devices of intermediate twist angles of 1.38° and 1.41°, in the vicinity of CNP, without any clear signs of superconductivity in these devices^{19,37}. In contrast, a third device with a twist angle of 1.44° - closer to the magic angle – exhibits superconductivity and OM. We used two independent probes to detect OM: (1) Hall effect measurements and (2) Josephson junctions. The OM signatures obtained from these methods are consistent with the Curie-Bloch equation and follow a power law that reveals a common magnetic ordering temperature of approximately 650 mK. Our sample uniquely exhibits a smaller energy scale for the symmetry broken state ($T_{OM2} \sim 650\text{mK}$) than that of the superconducting state ($T_{SC} \sim 1.3\text{K}$), see extended Fig. 5a and S6a. The JJ is dissipative at low temperatures and upon heating above T_{OM2} , resistance drops by orders of magnitude, and superconductivity prevails over OM. This indicates that the mechanism for spontaneous valley polarization-driven OM observed in our samples is likely different from the anomalous Hall effect observed at integer filling factors in twisted graphene systems^{21,23–25,34}.

We mapped out the phase space of OM as a function of the filling factor (ν) and displacement field (D). Extended Fig. 5a shows the general phase diagram of OM and SC as a function of ν and displacement field D . The OM is most prominent near the CNP and decreases as we approach $\nu = \pm 2$, where superconductivity emerges. As D increases, OM weakens while superconductivity becomes more robust, revealing a complementary relationship in their phase spaces. Using the Landau levels (LLs) of monolayer graphene (MLG) as a probe, we also demonstrated the variation in hybridization strength between the flat bands and Dirac cones as a function of D . Extended Fig. 5b shows the distribution of electron-doped superconductivity (e-SC), critical temperature (T_{SC}^e) and OM ordering temperature (T_{OM}) data points as a function of twist angle θ for alternating TTG devices taken from literature and this work. The green and purple colored phase space represents the e-SC and OM, respectively. The competition between magnetic and superconducting phases varies with the twist angle, resulting in a range around 1.4°, where superconductivity is suppressed at all densities while clear OM signatures persist. To further explore OM, we measured two additional TTG devices with twist angles of approximately 1.3° and 1.5°, which show no OM but exhibit superconductivity (see SI Section 3 and Fig. S9, S10, and S11 for further details).

In summary, our measurements reveal a rich phase diagram where both superconductivity and magnetic ordering appear, governed by carrier density, displacement field, and twist angle in TTG. These findings indicate that alternating TTG has a rather dissimilar phase diagram compared to TBG. The D -driven change in hybridization strength of flat bands with Dirac cone changes the ground state and dictates the stabilized correlated phase. The complementary phase space of OM to superconductivity might help explain the origin of superconductivity in TTG heterostructures. Particularly surprising is our finding that the usual sequence of energy scales is reversed in the TTG phase diagram, with superconductivity onsetting at higher temperatures than OM. Such behavior could, for example, result from critical triplet pairing fluctuations at the boundary of the superconductivity phase, giving rise to ferromagnetic correlations, which would constitute an intriguing role reversal compared to the typical phenomenology observed for competing instabilities. From a general physics perspective, the coexistence of magnetism and superconductivity within a single material platform is highly significant. This interplay opens exciting possibilities for realizing exotic quasiparticles in van der Waals-based hybrid devices, potentially advancing the search for non-abelian anyons and novel topological states.

References

1. Song, J. C. W., Shytov, A. V. & Levitov, L. S. Electron Interactions and Gap Opening in Graphene Superlattices. *Phys. Rev. Lett.* **111**, 266801 (2013).
2. Choi, Y. *et al.* Interaction-driven band flattening and correlated phases in twisted bilayer graphene. *Nat. Phys.* **17**, 1375–1381 (2021).
3. Bistritzer, R. & MacDonald, A. H. Moiré bands in twisted double-layer graphene. *Proc. Natl. Acad. Sci.* **108**, 12233–12237 (2011).
4. Wu, C., Bergman, D., Balents, L. & Sarma, S. D. Flat Bands and Wigner Crystallization in the Honeycomb Optical Lattice. *Phys. Rev. Lett.* **99**, 070401 (2007).
5. Iglovikov, V. I., Hébert, F., Grémaud, B., Batrouni, G. G. & Scalettar, R. T. Superconducting transitions in flat-band systems. *Phys. Rev. B* **90**, 094506 (2014).
6. Cao, Y. *et al.* Unconventional superconductivity in magic-angle graphene superlattices. *Nature* **556**, 43–50 (2018).
7. Park, J. M., Cao, Y., Watanabe, K., Taniguchi, T. & Jarillo-Herrero, P. Tunable strongly coupled superconductivity in magic-angle twisted trilayer graphene. *Nature* **590**, 249–255 (2021).
8. Hao, Z. *et al.* Electric field-tunable superconductivity in alternating-twist magic-angle trilayer graphene. *Science* **371**, 1133–1138 (2021).
9. Liu, J. & Dai, X. Orbital magnetic states in moiré graphene systems. *Nat. Rev. Phys.* **3**, 367–382 (2021).
10. He, M. *et al.* Competing correlated states and abundant orbital magnetism in twisted monolayer-bilayer graphene. *Nat. Commun.* **12**, 4727 (2021).
11. Wu, S., Zhang, Z., Watanabe, K., Taniguchi, T. & Andrei, E. Y. Chern insulators, van Hove singularities and topological flat bands in magic-angle twisted bilayer graphene. *Nat. Mater.* **20**, 488–494 (2021).
12. Nuckolls, K. P. *et al.* Strongly correlated Chern insulators in magic-angle twisted bilayer graphene. *Nature* **588**, 610–615 (2020).
13. Xie, Y. *et al.* Fractional Chern insulators in magic-angle twisted bilayer graphene. *Nature* **600**, 439–443 (2021).
14. Yazdani, A., Oppen, F. von, Halperin, B. I. & Yacoby, A. Hunting for Majoranas. *Science* **380**, eade0850 (2023).
15. Cao, Y. *et al.* Correlated insulator behaviour at half-filling in magic-angle graphene superlattices. *Nature* **556**, 80–84 (2018).
16. Lu, X. *et al.* Superconductors, orbital magnets and correlated states in magic-angle bilayer graphene. *Nature* **574**, 653–657 (2019).
17. Phong, V. T., Pantaleón, P. A., Cea, T. & Guinea, F. Band structure and superconductivity in twisted trilayer graphene. *Phys. Rev. B* **104**, L121116 (2021).
18. Cao, Y., Park, J. M., Watanabe, K., Taniguchi, T. & Jarillo-Herrero, P. Pauli-limit violation and re-entrant superconductivity in moiré graphene. *Nature* **595**, 526–531 (2021).
19. Lin, J.-X. *et al.* Zero-field superconducting diode effect in small-twist-angle trilayer graphene. *Nat. Phys.* **18**, 1221–1227 (2022).
20. Mukherjee, A. *et al.* Superconducting magic-angle twisted trilayer graphene hosts competing magnetic order and moiré inhomogeneities. *arXiv* (2024).
21. Sharpe, A. L. *et al.* Emergent ferromagnetism near three-quarters filling in twisted bilayer graphene. *Science* **365**, 605–608 (2019).
22. Sharpe, A. L. *et al.* Evidence of Orbital Ferromagnetism in Twisted Bilayer Graphene Aligned to Hexagonal Boron Nitride. *Nano Lett.* **21**, 4299–4304 (2021).
23. Serlin, M. *et al.* Intrinsic quantized anomalous Hall effect in a moiré heterostructure. *Science* **367**, 900–903 (2020).
24. Tseng, C.-C. *et al.* Anomalous Hall effect at half filling in twisted bilayer graphene. *Nat. Phys.* **18**, 1038–1042 (2022).
25. Stepanov, P. *et al.* Competing Zero-Field Chern Insulators in Superconducting Twisted Bilayer Graphene. *Phys. Rev. Lett.* **127**, 197701 (2021).
26. Zondiner, U. *et al.* Cascade of phase transitions and Dirac revivals in magic-angle graphene. *Nature* **582**, 203–208 (2020).
27. Saito, Y. *et al.* Isospin Pomeranchuk effect in twisted bilayer graphene. *Nature* **592**, 220–224 (2021).
28. Xie, M. & MacDonald, A. H. Weak-Field Hall Resistivity and Spin-Valley Flavor Symmetry Breaking in Magic-Angle Twisted Bilayer Graphene. *Phys. Rev. Lett.* **127**, 196401 (2021).
29. Christos, M., Sachdev, S. & Scheurer, M. S. Correlated Insulators, Semimetals, and Superconductivity in Twisted Trilayer Graphene. *Phys. Rev. X* **12**, 021018 (2022).
30. Shen, C. *et al.* Dirac spectroscopy of strongly correlated phases in twisted trilayer graphene. *Nat. Mater.* **22**, 316–321 (2023).
31. Bocarsly, M. *et al.* Imaging Coulomb interactions and migrating Dirac cones in twisted graphene by local quantum oscillations. *arXiv* (2024).

32. Díez-Mériá, J. *et al.* Symmetry-broken Josephson junctions and superconducting diodes in magic-angle twisted bilayer graphene. *Nat. Commun.* **14**, 2396 (2023).
33. He, W.-Y., Goldhaber-Gordon, D. & Law, K. T. Giant orbital magnetoelectric effect and current-induced magnetization switching in twisted bilayer graphene. *Nat. Commun.* **11**, 1650 (2020).
34. Zhang, N. J. *et al.* Angle-resolved transport non-reciprocity and spontaneous symmetry breaking in twisted trilayer graphene. *Nat. Mater.* **23**, 356–362 (2024).
35. Vries, F. K. de *et al.* Gate-defined Josephson junctions in magic-angle twisted bilayer graphene. *Nat Nanotechnol* **16**, 760–763 (2021).
36. Rodan-Legrain, D. *et al.* Highly tunable junctions and non-local Josephson effect in magic-angle graphene tunnelling devices. *Nat Nanotechnol* **16**, 769–775 (2021).
37. Mukherjee, A. *et al.* Superconducting magic-angle twisted trilayer graphene hosts competing magnetic order and moiré inhomogeneities.
38. Moshe, M., Kogan, V. G. & Mints, R. G. Edge-type Josephson junctions in narrow thin-film strips. *Phys Rev B* **78**, 020510 (2008).
39. Chen, S. *et al.* Current induced hidden states in Josephson junctions. *Nat. Commun.* **15**, 8059 (2024).

Methods

Stacking and Device fabrication

The TTG stack is prepared using dry-transfer method. The hBN and graphene flakes are exfoliated on clean Si/SiO₂ (285 nm) substrate. The number of graphene layers are determined by examining the FWHM of 2D peak Raman spectra (WITec alpha300 R) using 532nm laser. Monolayer graphene ~100 X30μm is cut into three pieces separated by ~5 μm gap using 1064nm Raman laser. The clean hBN crystals are examined using an optical microscope and dark field microscopy. The crystallographic axes of hBNs are determined using straight edges. Stamps for picking the flakes are prepared by placing polycarbonate (PC) thin films on polydimethylsiloxane (PDMS) dome stamps. The top hBN flake (~25nm) is picked at 100°C and the graphene flakes are picked up at 40°C. The transfer stage holding the Si chip with vacuum is rotated to ~1.45° and ~-1.45° to obtain the mirror-symmetric configuration of TTG. The bottom hBN (~30nm) is picked up at 50°C and the final stack dropped on clean Si/SiO₂ (285 nm) substrate at 180 °C. The melted PC on the stack is cleaned using chloroform and stack annealed in a vacuum at 350 °C to move the air bubbles, release strain, and remove impurities on top of the stack. The stack's contact mode cleaning and hBNs' thicknesses are determined using Bruker atomic force microscope. Jeol JBX9300-FS e-beam lithography is used to define metal top gates and JJs of lateral width~2μm. The Cr(4nm)/Au(16nm) metals are deposited with an e-gun evaporator for top gates. The edge contacts to graphene are made using CHF₃/O₂ plasma in RIE and consecutively depositing the Cr(2nm)/Au(65nm) metals in the angle rotator e-gun evaporator. The device is etched into Hall bar geometry using CHF₃/O₂ plasma in RIE.

Measurements

Bluefors LD400 dilution refrigerator with RC and RF filtering having base temperature~10mk is used to measure the transport characteristics. The Q-devil sample puck with additional filtering is used to mount the sample to the fridge. The four-probe measurements are performed using standard lock-in techniques using I_{ac} ~1nA rms (100MΩ resistor) and 11.377Hz frequency. The Femto voltage amplifiers are used at room temperature to amplify signals from fridge to SRS830 and SRS865A lock in amplifiers. Keithley 2400 source meters are used to apply top and bottom gate voltages. The bottom gate voltage (V_{bg}) and top gate voltage (V_{tg}) are converted to (n) and (D) using electrostatic equations $n = \frac{\epsilon_b \epsilon_0 (V_{bg} - V_{bo})}{ed_b}$ + $\frac{\epsilon_t \epsilon_0 (V_{tg} - V_{to})}{ed_t}$ and $D = \frac{\epsilon_b \epsilon_0 (V_{bg} - V_{bo})}{d_b} - \frac{\epsilon_t \epsilon_0 (V_{tg} - V_{to})}{d_t}$ (ϵ_b, ϵ_t dielectric constant of bottom and top hBN ~ 3.6 ; ϵ_0 : permittivity of air; e : charge of electron; d_b, d_t : thickness of bottom (30nm) and top hBN (25nm); V_{bo}, V_{to} are the bottom and top gate voltages of charge neutrality point at zero magnetic field). From the Landau fan diagram of R_{xx} and R_{yx} we find the moiré superlattice carrier density $n_s = 4.65 \times 10^{12} \text{cm}^{-2}$, $4.72 \times 10^{12} \text{cm}^{-2}$ and $4.80 \times 10^{12} \text{cm}^{-2}$ corresponding to the twist angle of 1.38°, 1.41° and 1.44° using equation $n_s = 8\theta^2 / \sqrt{3} a^2$ ($a=0.234\text{nm}$), see supplementary section 1 for more information. AMI 9-1-1 vector magnet is used to study magnetic field direction dependence on R_{yx} . For dV/dI measurements AC excitation voltage of ~0.1V rms is applied using lock in amplifier and dc bias voltages is applied using Yokogawa voltage source meter through 100MΩ resistor.

Analysis of Hall data and fittings: We calculated Hall carrier density using equation, $n_H = 1/e * \frac{dR_{xy}}{dB_z}$, (here, e is elementary charge), the $\frac{dR_{xy}}{dB_z}$ is calculated at low B_z range : $-0.1\text{T} \leq B_z \leq 0.1\text{T}$. The high B_z range: $-0.5\text{T} \leq B_z \leq 0.5\text{T}$ fitted data is shown in SI Fig. S2. The amplitude of R_{xy} slope *w.r.t* B_z shown in extended Fig 2 is calculated by subtracting linear slope of R_{xy} vs B_z from $\frac{dR_{xy}}{dB_z}$. To quantify the change in the v_F with displacement field, we estimate Fermi energy

E_F by employing a single-particle equation for the MLG LL_s spectrum, $E_F = \text{sgn}(L_n)v_F\sqrt{(2e\hbar |L_n| \times B)}$; where L_n is Landau level index, v_F is Fermi velocity of the monolayer Dirac cone, e is the elementary charge, and \hbar is reduced Planck's constant. First, we calculated E_F for LL_1 at $D=0\text{V/nm}$ as $\sim 8\text{meV}$ at $\nu \sim 0.45$, $\sim 4\text{meV}$ at $\nu \sim 0.10$ and $\sim 1\text{meV}$ at $\nu \sim 0.70$ by using $v_F = 10^6\text{m/s}$, see SI Fig S3 for more details. Since E_F is constant for given LL , the change in curvature is used to estimate v_F change with the displacement field. The R_{xy} jump amplitude as a function of dc bias current is fitted to the Curie Bloch equation using non-linear least square fitting method.

Josephson junction analysis: The phase space of JJ as a function of the top gate and the back gate is shown in extended Fig 4. The carrier density (n_j) and displacement field (D_j) across JJ is calculated using electrostatic equations $n_j = \frac{\epsilon_b\epsilon_0(V_{bg}-V_{bo})}{ed_b}$ and $D_j = \frac{\epsilon_b\epsilon_0(V_{bg}-V_{bo})}{d_b}$ (ϵ_b dielectric constant of bottom ~ 3.6 ; ϵ_0 : permittivity of air; e : charge of electron; d_b : thickness of bottom (30nm); V_{bo} are the bottom gate voltages of charge neutrality point at zero magnetic field). The moiré filling factor ν_j of JJ is calculated using the equation $\nu_j = n_j/n_s$ corresponding to $n_s = 4.80 \times 10^{12}\text{cm}^{-2}$. The diode effect at $B_z = 0T$ is measured using 1nA ac excitation and switching dc bias current between superconducting critical current I_C ($dV/dI=0\ \Omega$) and $-I_C$. The Curie Bloch equation is fitted to the η and resistance using the non-linear least square fitting method.

Data and materials availability:

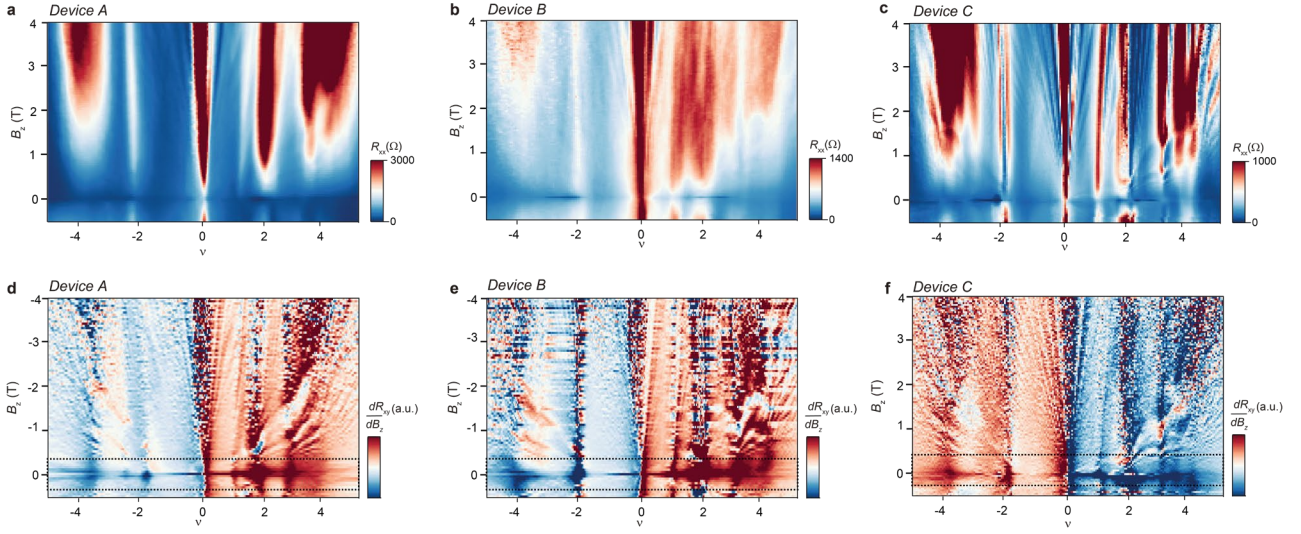
The data supporting the findings in this paper are available from the corresponding author on reasonable request.

Acknowledgements: We thank Eli Zeldov and Patrick Ledwith for fruitful discussions. V.B. acknowledges support from the Dean of the Faculty. Y.R. acknowledges the support from the Quantum Science and Technology Program 2021, the Schwartz Reisman Collaborative Science Program, supported by the Gerald Schwartz and Heather Reisman Foundation, the Minerva Foundation with funding from the Federal German Ministry for Education and Research, and the European Research Council Starting Investigator Grant Anyons 101163917.

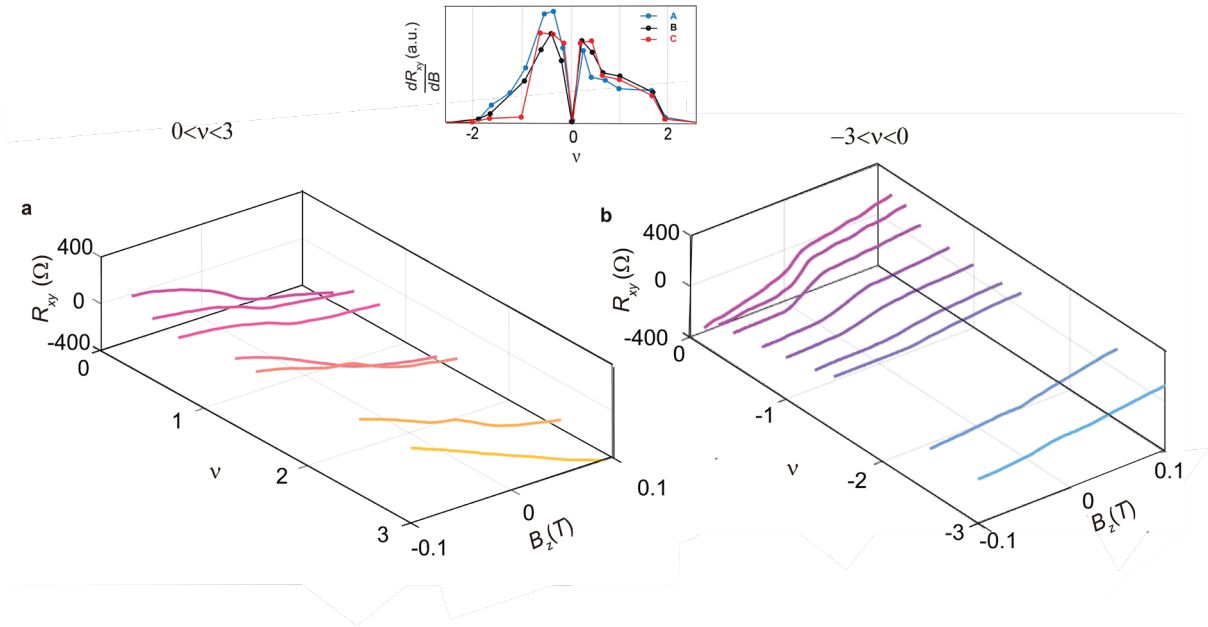
Author contributions: V.B. stacked and fabricated the device. L.R. and Y.R. helped design and improve the device quality. K.W. and T.T. grew the hBN crystals. V.B. L.A. and L.R. set up the fridge and developed the measurement codes. V.B. and L.R. performed the measurements. A.I. prepared the schematic illustrations of the devices. V.B., L.R., L.A., M.B., G.S., Y.O., T.H., and Y.R. contributed to the analysis of the results. V.B., L.R., and Y.R. wrote the paper with input from all coauthors. Y.R. supervised the overall work done on the project

Competing interests: The authors declare no competing interests.

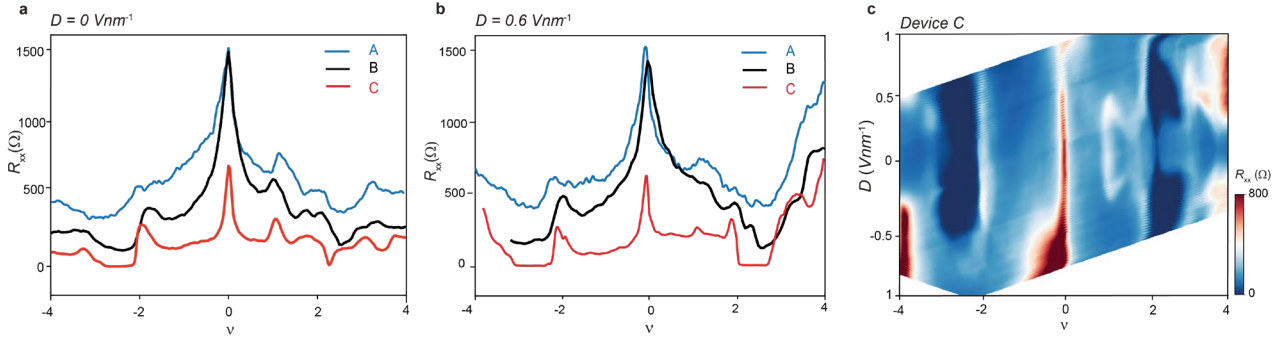
Extended Figures:



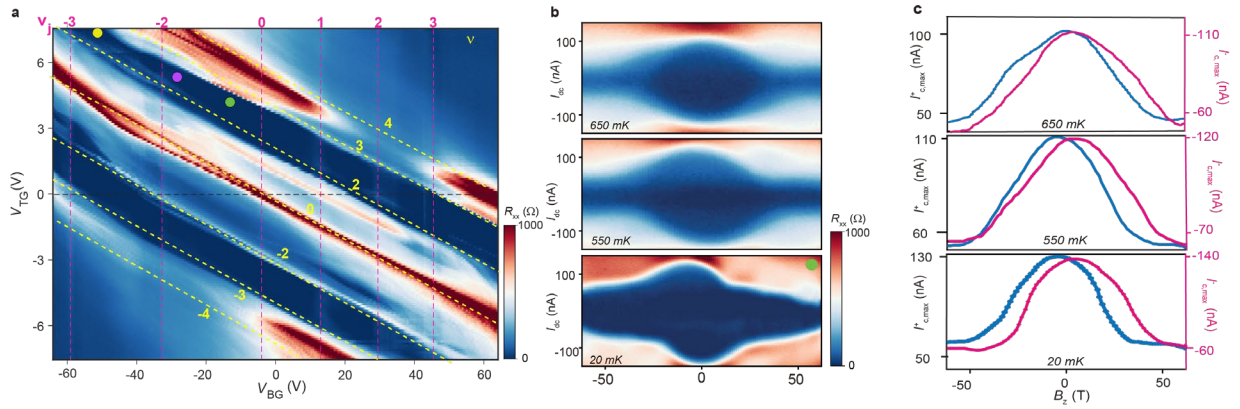
Extended figure 1: The Landau fan diagrams of R_{xx} and R_{xy} . Measurements are taken at 15mK and $D=0\text{V/nm}$ for device (a) A (contacts 2-3) (b) B (contacts 14-13) and (c) C (contacts 6-7). The Landau fan diagram of $\frac{dR_{xy}}{dB_z}$ measured at 15mK and $D=0\text{V/nm}$ for device (a) A (contacts 15-3) (b) B (contacts 14-4) and (c) C (contacts 11-6). Dashed black boxes show the slope change in $\frac{dR_{xy}}{dB_z}$ around $B_z=0\text{T}$.



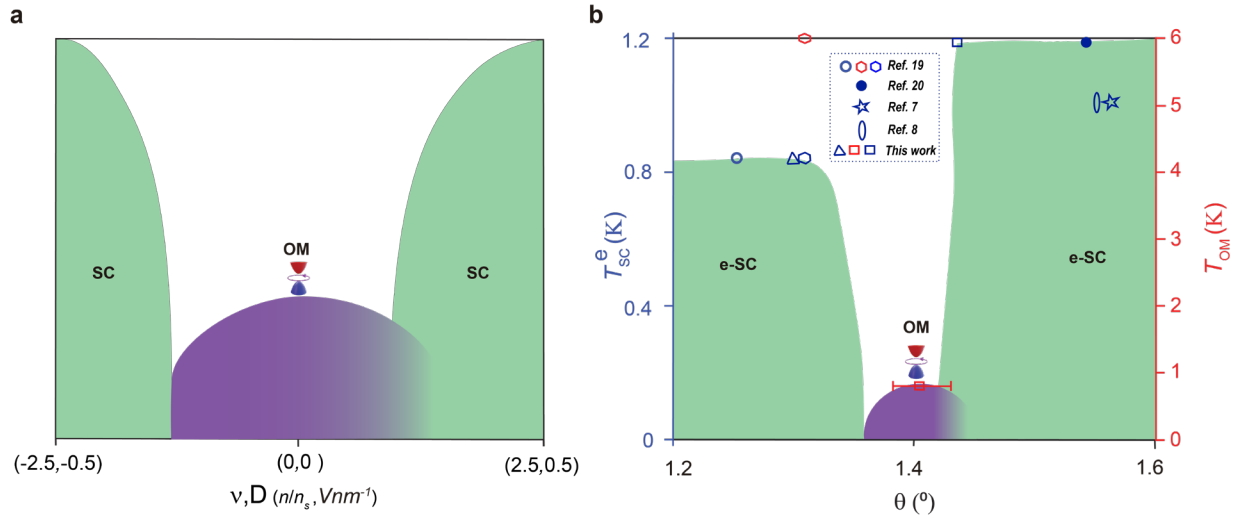
Extended figure 2: Evolution of jumps in R_{xy} as a function of ν for electron and hole-doped regions. Line cuts of R_{xy} vs B_z for (a) electron and (b) hole doping at $D=0\text{V/nm}$ for device A. Inset shows the variation of $\frac{dR_{xy}}{dB_z}$ amplitude around $B_z=0$ extracted after subtracting the linear slope of R_{xy} at high B_z as a function of filling factor ν for all three devices. Maxima is obtained in vicinity to CNP on hole doping side.



Extended figure 3: Evolution of superconductivity with twist angle. Line cuts of R_{xx} vs ν for all three devices at $T=20\text{mK}$ and $D =$ (a) 0V/nm and (b) 0.6V/nm . (c) D vs ν phase space of R_{xx} for device C, at $T=20\text{mK}$.



Extended figure 4: Phase space of Josephson junction and temperature dependence of Fraunhofer asymmetry. (a) Phase space of R_{xx} for top gate (V_{TG}) vs back gate voltage (V_{BG}) across the JJ2 at 20mK . The slanted dotted yellow lines correspond to the filling factor (ν) of regions with both top and back gate *i.e* left and right sides of the JJ. The vertical pink dotted lines correspond to the filling factor of the weak link (ν_j) region with no top gate. (b) The Fraunhofer pattern measured at $\nu_j \sim -0.45$ forming $S|OM|S$ JJ at 20mK , 500mK and 650mK . (c) Line cuts of the maximum critical current extracted from figure b.



Extended figure 5: Phase diagrams of superconductivity and orbital magnetism as a function of twist angle, density and displacement field. (a) General phase diagram of SC and OM with ν and displacement field D . The OM is stronger near D (ν)=0, and gets weaker as we move away, whereas SC is weaker (absent) near D (ν)=0 and gets stronger as we move away. **(b)** Phase space of critical temperature of electron doped superconductivity (e-SC) T_{SC}^e (blue data points, corresponding to left y axis) and OM ordering temperature T_{OM} (red data points corresponding to right Y axis) as a function of twist angle θ for alternating TTG devices. The OM peaks around 1.40° and is flanked by e-SC domes on lower and higher angles.

Supplementary information

Competing Orbital Magnetism and Superconductivity in Twisted Trilayer Graphene Moiré Superlattice

Vishal Bhardwaj¹, Lekshmi Rajagopal¹, Lorenzo Arici¹, Matan Bocarsly¹, Alexey Ilin¹, Gal Shavit⁵, Kenji Watanabe³, Takashi Taniguchi⁴, Yuval Oreg¹, Tobias Holder⁶, Yuval Ronen^{1*}

¹Department of Condensed Matter Physics, Weizmann Institute of Science, Rehovot 7610001, Israel

³Research Center for Functional Materials, National Institute for Materials Science, Tsukuba 305-0044, Japan

⁴International Center for Materials Nanoarchitectonics, National Institute for Materials Science, Tsukuba 305-0044, Japan

⁵Department of Physics and Institute for Quantum Information and Matter, California Institute of Technology, Pasadena, California 91125, USA

⁶School of Physics and Astronomy, Tel Aviv University, Tel Aviv 69978, Israel

*yuval.ronen@weizmann.ac.il

1. Stacking and fabrication of device

The stacks are prepared using flakes exfoliated on Si/SiO₂ substrates. The dome shaped stamps are prepared using polydimethylsiloxane (PDMS) and 6% (by weight) polycarbonate (PC) solution dissolved in chloroform. A big monolayer of graphene around 100×30um is identified using optical microscope and further confirm by analyzing 2D peak of Raman spectra (532nm laser of Witec Raman system). Raman 1064nm laser is used to cut the monolayer into 3 pieces of ~30um length. The hBNs are also exfoliated on Si/SiO₂ and clean areas are identified using optical microscope. The stack is prepared using commercial transfer stage. The top hBN of thickness ~ 25nm is picked at 100° C by Z movement of the stamps. The first graphene layer is picked at 40° C also using Z movement of the stamp. The stage is rotated to around +1.45° and second layer is also picked at same parameters. Subsequently the stage is rotated to -1.45° and third layer is picked. The bottom hBN (~30nm) is picked at 50° C using Z movement of stamps, the stamp wavefront is moved away from stack area and the stage temperature is raised to 180° C to melt the PC with stack on chip. The stack is cleaned using chloroform to remove PC residues. The stack is annealed at 350° C for 2hr in vacuum furnace with base pressure of 5×10⁻⁸ Torr to release strain and remove any residues on top of stack. The flake thickness is measured, and the topography of stack is cleaned using Bruker AFM. See fig. S1 (a) for a 100X resolution picture of the stack before nanofabrication. The Jeol JBX 9300FS e-beam lithography is used to prepare Hall bar geometry. Double layer PMMA is used in every step of nano fabrication. In the first step, metal top gate is deposited with Cr (5nm) Au (20nm) using e-gun evaporator. In the second step, stack etching is performed using CHF₃/O₂ gas mixture in reactive ion etching machine. Metal bridges (Ti (25nm)/Au (250nm)) are prepared to avoid shorting of top gate leads to the graphene at the edges of stack. The edge contacts to the graphene are made by first etching stack using CHF₃/O₂ gas and subsequently depositing Cr (2nm)/ Au (65nm) metals on 15° angle using e-gun evaporator while rotating the sample holder. The final device consists of three Hall bar devices A, B and C. There are two Josephson junctions, first between device A and B of width

~200nm (JJ1) and second between device B and C of width ~100nm (JJ2). See fig. S2 (b) for the image of the final device, after fabrication process.

The transport properties are measured in LD400 Bluefors dilution refrigerator. The fridge has thermo-coax lines and low pass RC and RF filters. It has 9-1-1 magnet with base temperature of 7mK. Standard 830SRS and 865SRS lock in amplifiers are used to measure transport properties. Femto DLPVA-101-F-D room temperature voltage amplifiers (1TΩ input impedance) are used before feeding signal to lock in amplifiers. Keithley 2400 voltage source meters are used for controlling voltages of gates. For dV/dI characteristics, Yokogawa is used as dc source meter and lock in as AC source. The carrier density (n) and displacement field (D) are calculated using electrostatics equations $n = \frac{\epsilon_b \epsilon_0 V_{bg}}{ed_b} + \frac{\epsilon_t \epsilon_0 V_{tg}}{ed_t}$ and $D = \frac{\epsilon_b \epsilon_0 V_{bg}}{d_b} - \frac{\epsilon_t \epsilon_0 V_{tg}}{d_t}$ respectively. Here, ϵ_0 is the dielectric constant of vacuum and is equal to $8.854 \times 10^{-12} \text{ CV}^{-1}\text{m}^{-1}$, ϵ_t (ϵ_b) are the relative dielectric constant of the top (bottom) hBN ~ 3.9 , d_t (d_b) are thickness of the top hBN (Si/SiO₂ +bottom hBN) which we estimated to be 25 nm (285nm +30 nm), V_{tg} (V_{bg}) are the voltages of top (bottom) gates. The moiré super lattice carrier density (n_s) for device A, B and C are 4.4×10^{12} , 4.65×10^{12} and $4.8 \times 10^{12} \text{ cm}^{-2}$ respectively. The twist angles are estimated using equation $n_s = 8\theta^2 / \sqrt{3} a^2$ ($a=0.234\text{nm}$) and are found to be 1.38° , 1.41° , and 1.44° for A, B and C device, respectively.

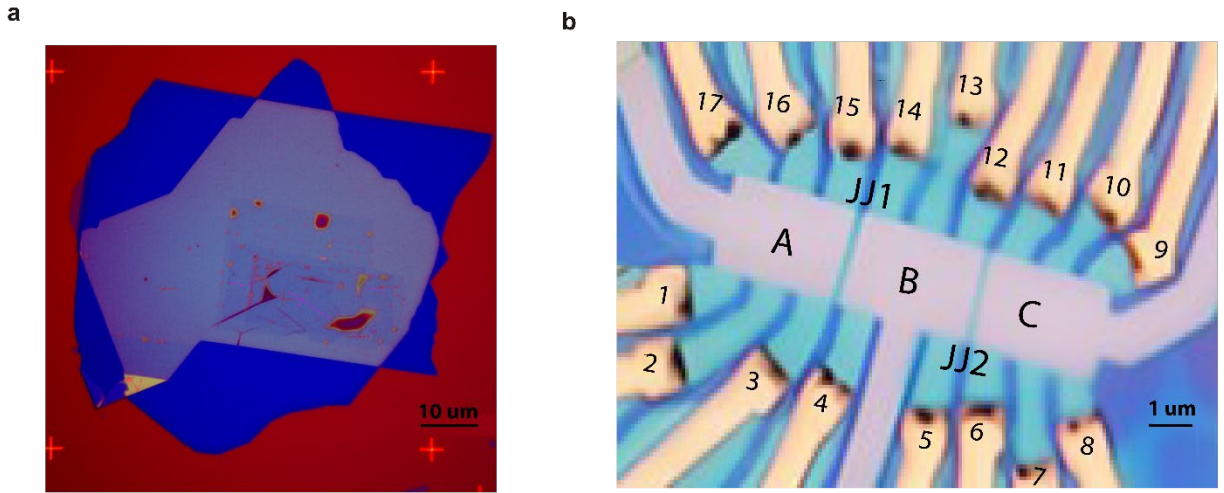


Figure S1: (a) 100X zoomed optical image of the stack before nanofabrication. Color scale is 10μm. **(b)** Optical image of the final devices after nanofabrication. The Josephson junctions, JJ1 and JJ2 have weak link of ~200nm and 100nm respectively. The width of the Hall bar is ~2μm, see the scale ~1μm.

2. Transport characterization of hall bar devices:

When we dope, the electrons (holes) to the conduction (valence) bands of the TTG are distributed between the flat bands and ML Dirac cone. Most of the charge carriers are filled in the flat bands due to high density of state (DOS) and the rest goes to ML Dirac cone^{1,2}. The mini-Brillouin zone of TTG has four-fold degenerate bands with flavors $K, K', \uparrow, \downarrow$. When we start doping electrons(holes) from $\nu=0$, all four flavors start filling the conduction (valence) bands equally, and hence a linear (unity) slope between Hall carrier density (n_H) and ν is expected in the vicinity of CNP³. At $\nu=\pm 1$ (± 3),

the symmetry of four-fold degenerate bands breaks and out of four anyone (three) flavor is filled completely which result in resets towards zero. Similarly at $\nu=\pm 2$, due to symmetry breaking of spin and valley isospin degenerate bands, two flavors of either spin or valley isospin are filled completely, and a reset is observed. At $\nu=\pm 4$ all four flavors are filled and Fermi energy (E_F) exits the flat bands and we observe reset toward zero again. This symmetry breaking of degenerate bands results in Chern insulator states at integer ν , as seen in Landau fan diagrams of R_{xx} and R_{xy} at $D=0\text{V/nm}$ (see extended Fig1).

We calculated the normalized Hall carrier density using equation $\nu_H = 1 / (e * \frac{dR_{xy}}{dB_z} * n_s)$; (here, e is elementary charge, n_s moiré superlattice density), the $\frac{dR_{xy}}{dB_z}$ is calculated at low B_z range ($-0.1\text{T} \leq B_z \leq 0.1\text{T}$) and high B_z range ($-0.5\text{T} \leq B_z \leq 0.5\text{T}$) around $B_z=0\text{T}$. The variation of quantity $(\nu_H - \nu)$ with ν shed light on the evolution of TTG DOS with varying E_F ^{4,5}. Fig. S2 (a) and (b) shows the $(\nu_H - \nu)$ vs ν plot for high B (red) and low B (blue) ranges at $D=0\text{V/nm}$ and 0.6V/nm , respectively. The integer values of $(\nu_H - \nu)$ are expected at integer ν corresponding to symmetry breaking and we observe this condition at $\nu=+1, \pm 2, +3$ and ± 4 , see red curve in fig. S2 (a). However, in addition to that a pronounced kink is observed in the vicinity of CNP towards hole doping and two small kinks are observed just before $\nu=+2$ and -2 as shown by black arrows in fig. S2 (a). These kinks are also associated with the symmetry breaking of flavors and presence of isospin ferromagnetic state^{5,6}. The behavior of sample at high displacement field looks completely different, as seen in fig. S2 (b). The kinks near the CNP vanishes and strong van hove singularities are observed at $\nu=\pm 2$ and $\nu=\pm 3$, i.e. on the boundary of superconductivity region. This signifies the strengthening of superconductivity at high displacement field in $2 \leq |\nu| \leq 3$ ⁴. The Landau fan diagrams of $\frac{dR_{xy}}{dB_z}$ at high displacement fields (0.6V/nm) is shown in fig. S2(c-d) for devices A and C respectively. The jumps in R_{xy} around $B_z=0$ in both devices has vanished. An interesting note is that in Device C ($\theta = 1.44^\circ$), $\nu=3$ becomes visible which is absent in device A ($\theta = 1.38^\circ$).

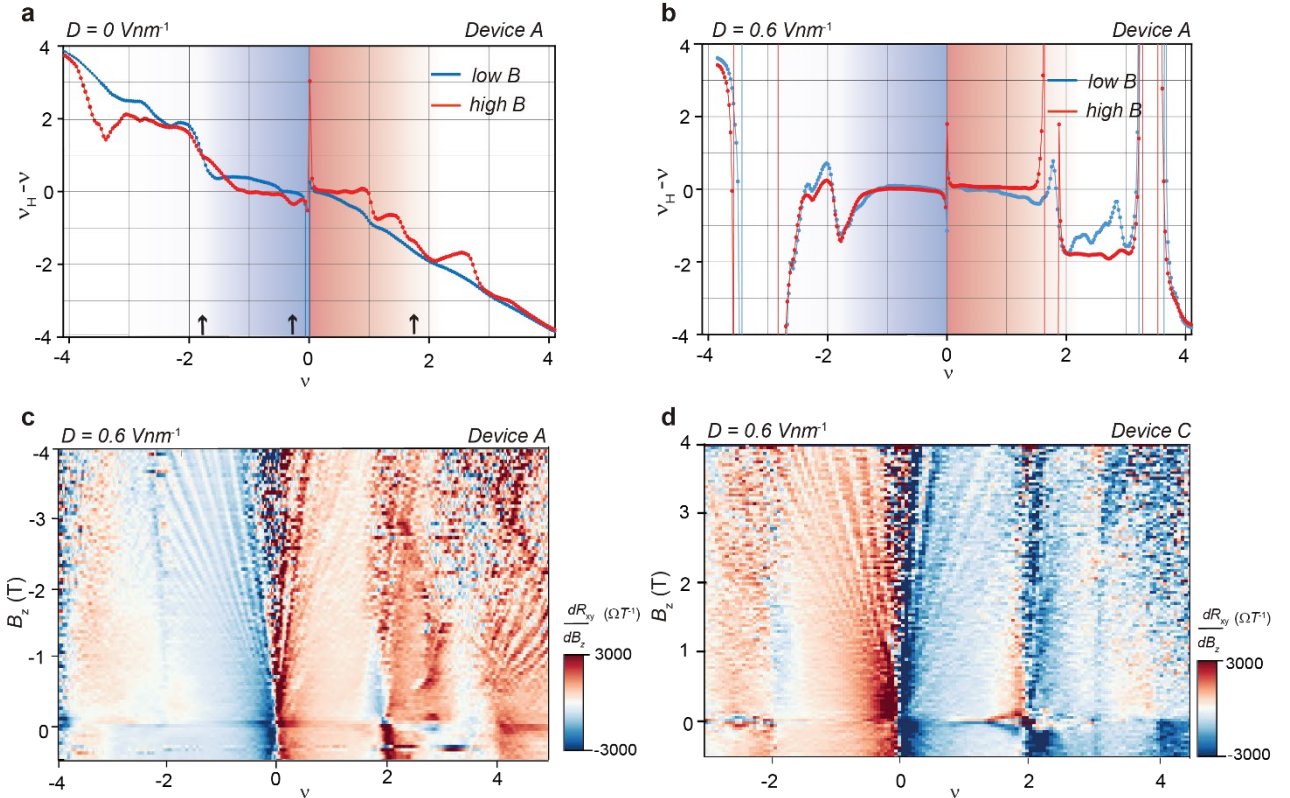


Figure S2: The moiré filling factor (ν) subtracted from renormalize Hall density $\nu_H = B_z / e\rho_{xy}n_s$ vs ν plots at low B_z ($-0.1\text{T} \leq B_z \leq 0.1\text{T}$) and high B_z ($-0.5\text{T} \leq B_z \leq 0.5\text{T}$) shown by blue and red colors, respectively at (a) $D=0\text{V/nm}$ and (b) $D=0.6\text{V/nm}$. Landau level fan diagram of $\frac{dR_{xy}}{dB_z}$ at $D=0.6\text{V/nm}$ for device (c) A and (d) C.

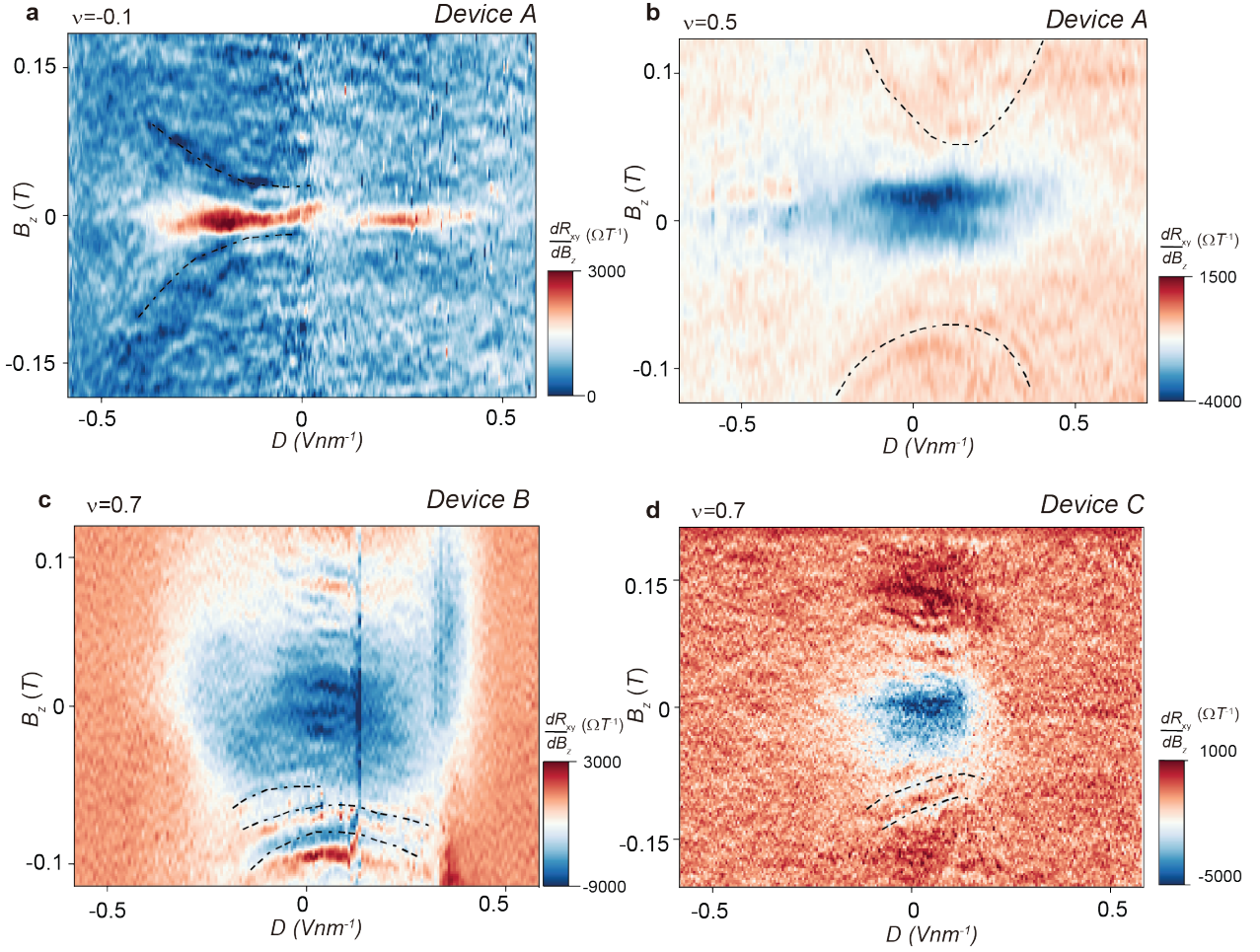


Figure S3: The 2D plots of $\frac{dR_{xy}}{dB_z}$ for B_z vs D at fixed (a) $\nu=-0.1$ (device A), (b) $\nu=0.5$ (device A) (c) $\nu=0.7$ (device B) and (d) $\nu=0.7$ (device C).

The TTG band structure consist of flat bands of TBG at $\sqrt{2}$ times the twist angle and a bystander monolayer Dirac cone. The mirror symmetric configuration of TTG means the localization of wavefunction on top/bottom layers can be tuned by the application of displacement field. At $D=0\text{V/nm}$, flat bands and Dirac cone are decoupled, however with application of D the flat bands and Dirac cone start hybridizing. This hybridization can result in rich physics. Here we are utilizing

the ML Dirac cone Landau levels and their hybridization as a probe to estimate the E_F of flat bands^{1,2}. We observe large value of $\left|\frac{dR_{xy}}{dB_z}\right|$ near by $B_z = 0T$ due to orbital magnetism (OM) which disappear with the increase in hybridization (D). The parabolic shaped curves in the figures represent the Landau levels (LL_s) of monolayer graphene at constant Fermi energy (E_F) defined by ν . The most prominent feature is the upward curvature of these curves with increasing D , which results from the hybridization between the MLG Dirac cone and the flat bands¹. As D , and therefore hybridization increases, the slope of the MLG Dirac cone, *i.e.* Fermi velocity, $v_F = dE/dk$ decreases. Since E_F is fixed, the LL_s appear at higher B . To quantify the change in the v_F , we estimate Fermi energy E_F by employing a single-particle equation for the MLG LL_s spectrum, $E_F = \text{sgn}(L_n)v_F\sqrt{(2e\hbar |L_n| \times B)}$; where L_n is Landau level index, v_F is Fermi velocity of the monolayer Dirac cone, e is the elementary charge, and \hbar is reduced Planck's constant. We estimated $E_F \sim 8\text{meV}$ for LL_1 and $\sim 9\text{meV}$ for LL_2 at $\nu \sim -0.45$ (see Fig 2 (a) main file) and $E_F \sim 4\text{meV}$ at $\nu \sim -0.10$ we, see fig. S3(a). As we tune E_F to electron doped $\nu \sim 0.70$ we estimated $E_F \sim 11\text{meV}$ for LL_1 and $E_F \sim 13\text{meV}$ for LL_2 , see Fig 2 (b) main file. These values of E_F at corresponding ν matches exactly with the estimation made using squid on tip scanning experiments¹. The upward curvature of LL_s lines with D indicate the hybridization of monolayer Dirac cone with flat bands, with the increase in D the slope of dE/dk decreases and hence v_F decreases, since the E_F is fixed the LL_s are observed at higher B_z in higher D . The estimated v_F change at $\nu = -0.10$ and -0.45 is $\sim 67\%$ and 45% for D change from 0 to 0.5V/nm . At $\nu = 0.70$ v_F change by $\sim 15\%$ for D change from 0 to 0.25V/nm .

Fig. S4 (a) and (c) shows the R_{xy} jumps in forward and backward sweeping of magnetic field at $\nu = -0.45$ and $\nu = 0.7$ respectively at $D = 0\text{ V/nm}$. We note the absence of hysteresis in these plots, despite the presence of a clear jump. The corresponding $R_{xy} - B_z$ sweeps at higher displacement, $D = 0.6\text{ V/nm}$ shows that these jumps have vanished, see fig. S4 (b) and (d). We explicitly show the dependence of R_{xy} jumps in 0° to 90° direction of the applied magnetic field $(B_x^2 + B_z^2)^{1/2}$ for device B and C respectively in fig. S5 (a) and (b). The R_{xy} jumps are present in all devices but are most prominent in device A (main fig. 3 and extended fig. 2) and decreases as we move to twist angles closer to the magic angle. We characterize the SC in our near magic angle device, Device C. From R_{xx} -T plot of Device C, $T_C \sim 1.3\text{ K}$ estimated corresponding to the 90% drop in resistance, see fig. S6 (a). We show the linecuts of dV/dI characteristics of the JJ2 taken at $B_z = 0\text{G}$, with configuration S|X|S, where S corresponds to $\nu \sim 2.7$ and X corresponds to ν_j , which is varied from ~ -3 to 2.5 . We see asymmetry in the dV/dI w.r.t I_{dc} in ν_j close to the CNP, but this dies off at higher ν_j . See fig. S6(b). Figure S6 (c) shows the temperature dependence of dV/dI characteristics across the JJ2 at $\nu_j = -0.45$. The curve becomes approximately symmetric at 650mK .

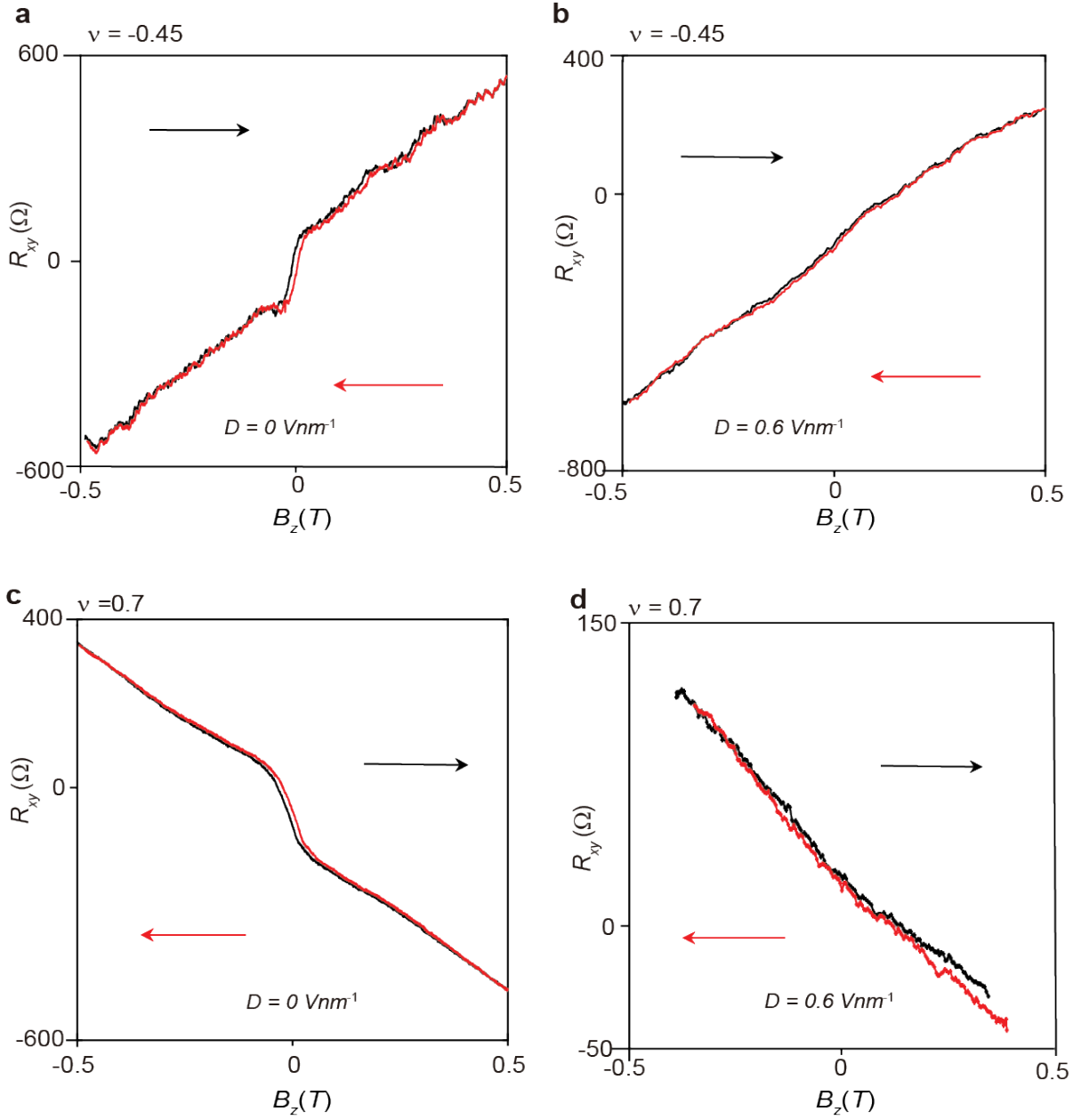


Figure S4: Line cuts of R_{xy} for B_z sweep directions -0.5T to 0.5T (black) and 0.5T to -0.5T (red) at **(a)** $\nu = -0.45$, $D=0\text{V/nm}$, **(b)** $\nu = -0.45$ and $D=0.6\text{V/nm}$; **(c)** $\nu=0.70$, $D=0\text{V/nm}$ and **(d)** $\nu = 0.70$ and $D=0.6\text{V/nm}$ for device A.

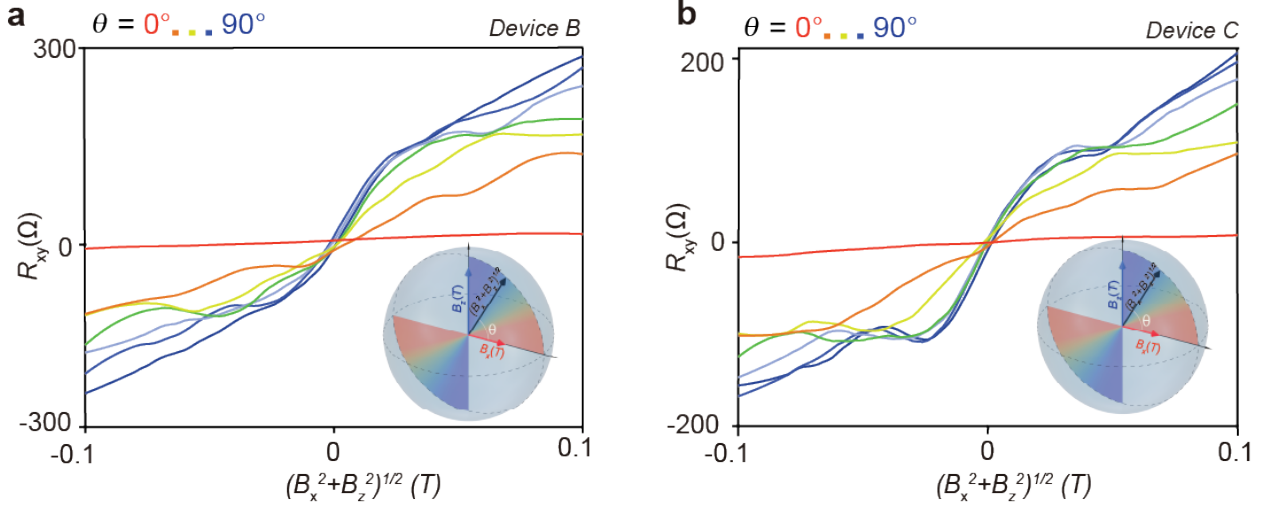


Figure S5: The R_{xy} vs $B = (B_x^2 + B_z^2)^{1/2}$ at varying θ between sample and B from 90° (blue) to 0° (red) in steps of 15° measured at 15mk for (a) device A and (b) device B.

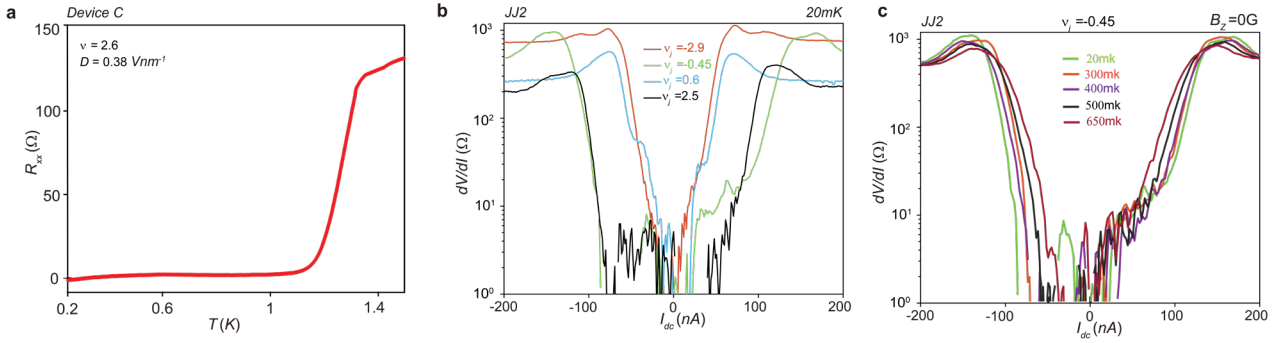


Figure S6: (a) The R_{xx} - T plot of device C measured at $B_z = 0T$, $\nu=2.35$ and $D=0.42V/nm$. (b) The dV/dI vs I_{dc} characteristics for SC state tuned to $\nu \sim 2.7$ across JJ2 and weak link tuned to different ν_j shown in figure legends. (c) Temperature dependence of dV/dI vs I_{dc} characteristics $\nu_j \sim 0.45$ across JJ2.

We can switch between superconducting (SC) and non-SC states by alternating I_{dc} between $\pm I_c^-$ on the asymmetric curve of dV/dI at $B_z=0$ G. Fig. S7a shows the dV/dI (Ω) characteristics measured by alternating between I_c^- ($dV/dI=0$ Ω) and $-I_c^-$ every 20 seconds and plotted over time in the temperature range 20mK to 650mK. The resistance R in the non-SC state decreases with increasing temperature. We fitted the temperature dependence of R to a Curie Bloch law, viz. $R = m(1 - T/T_{OM3})^\gamma$, and estimated $m = 30.05 \pm 1.5 \Omega$, $\gamma \sim 0.24 \pm 0.05$ and $T_{OM3} \sim 650$ mK as seen in Fig. S7b. The exponent of Curie Bloch law is expected to contain information about the magnetic moments, for example for a magnetic state of 2D Ising nature a critical exponent of 0.125 is expected^{7,8}. However, in our case we measure the exponent 0.24 ± 0.05 from resistance of the diode-like effect, 0.45 ± 0.05 from the R_{xy} data and 0.6 ± 0.2 from the asymmetry in critical currents. The scaling behaviors are consistent provided the resistance of diode effect is coupled to $\sim M^2$, R_{xy} to $\sim M^3$ and η to $\sim M^4$ ^{9,10}. However, we believe a microscopic picture is needed to clarify this point.

We show the Fraunhofer patterns in two e - h Josephson junction configurations, Fig. S7 (a) $S^+|OM|S^-$ and (b) $S^+|N|S^-$ in JJ2, here S^+ and S^- correspond to h and e side SC, respectively. We see that while $S^+|N|S^-$ ($\nu_L = -2.5$, $\nu_j = 1.8$, $\nu_R \sim 2.7$) shows a clear Fraunhofer pattern with clear dips in interference, we do not see a clear pattern in $S^+|OM|S^-$

($v_L = -2.4$, $v_j = 0.5$, $v_R \sim 2.7$). Moreover, the weak Fraunhofer is also slightly asymmetric about $I_{dc} = 0$, owing to the OM.

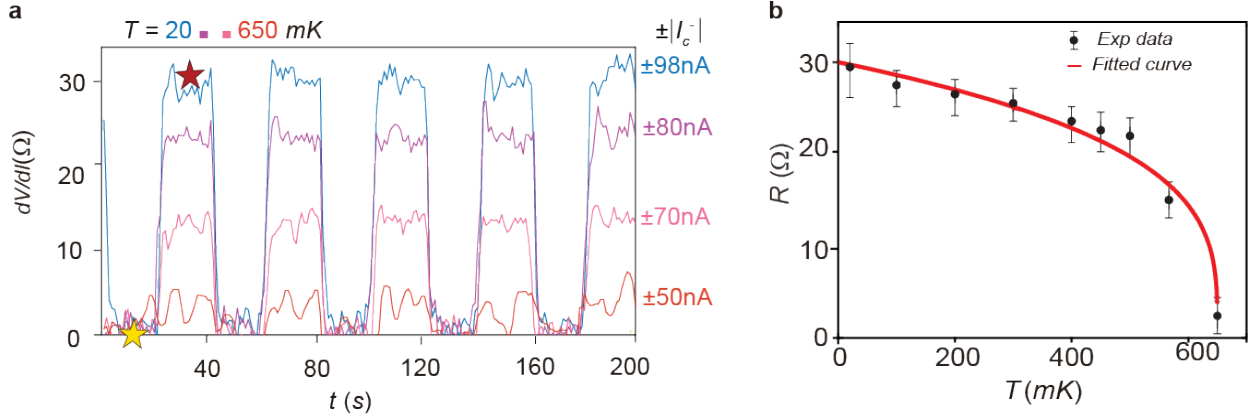


Figure S7: (a) The dV/dI (Ω) characteristics of S|OM|S JJ measured at $B_z=0$ G while alternating I_{dc} between I_c^- ($dV/dI=0$ Ω , SC state) and $-I_c^-$ (non-SC) after every 20 seconds in a temperature range of 20mK to 650mK. (b) Resistance of the non-SC state (R) calculated from Fig 4e and plotted as a function of temperature (black data points). The red line corresponds to fits of the Curie Bloch equation $\Delta R = m(1 - T/T_{OM3})^Y$. The error bars depict the standard deviations in R .

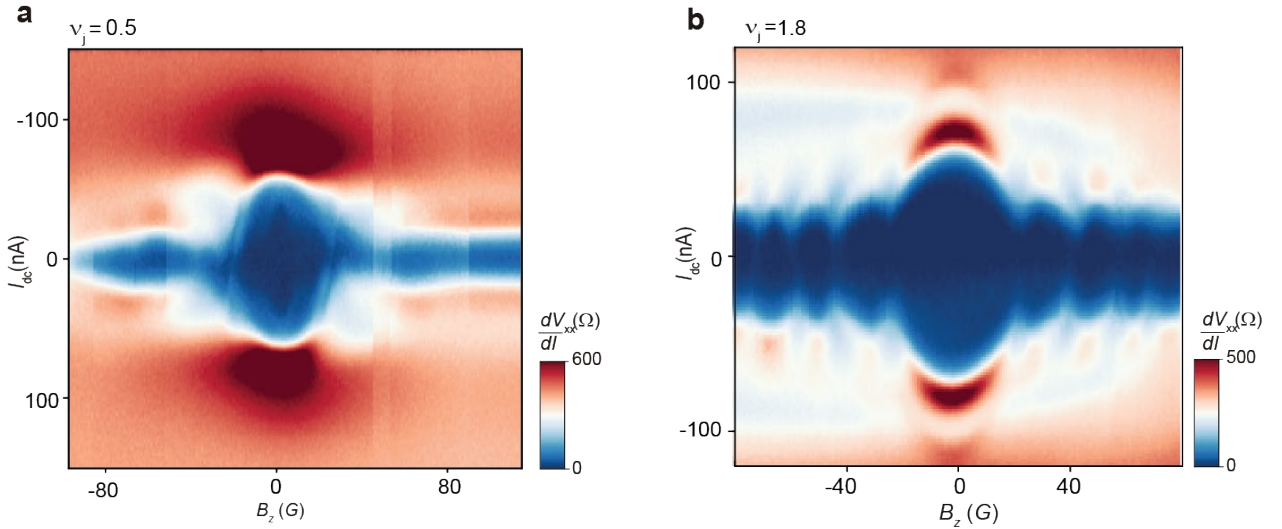


Figure S8: The Fraunhofer pattern measurements at (a) The S|OM|S JJ configuration ($B_G=3.8$ V, $T_{gL}=-4.4$, $T_{gR}=2.8$) the left side of JJ SC state tuned to $v_L \sim -2.5$, right side SC $v_R \sim 2.7$ and weak link tuned $v_j \sim 0.5$. (b) The S|N|S JJ configuration ($B_G=27.6$ V, $T_{gL}=-6.2$, $T_{gR}=0.7$) corresponding to hole side SC on left side (S $^{\prime}$) $v_L \sim -2.4$ and electron side SC on right side (S $^{\prime\prime}$) $v_R \sim 2.7$ of the JJ with weak link tuned to $v_j \sim 1.8$.

3. Transport characteristics of devices with 1.3° and 1.5° twist angles

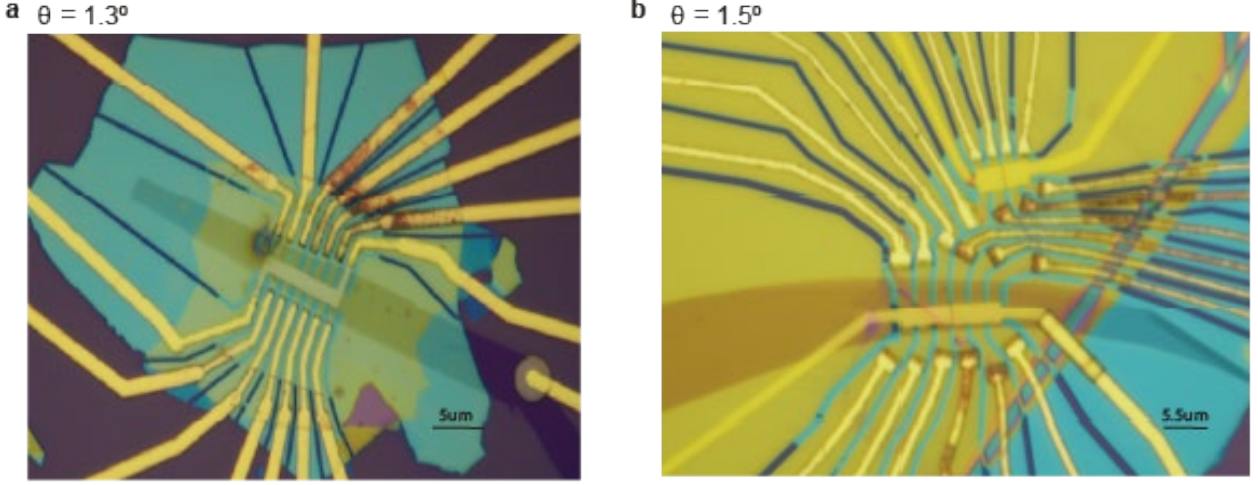


Figure S9: The additional TTG devices with twist angles **(a)** 1.3° and **(b)** 1.5°.

We stacked two other samples with twist angle 1.30° and 1.50° to explore OM in region above and below 1.40° regime, see fig. S8. Sample with 1.30° twist angle has top hBN~32nm and bottom hBN~55nm thickness. This sample has graphite as bottom gate. Sample with twist angle 1.50° has top hBN~60nm and bottom hBN~36 nm. This sample has two different Josephson junction devices, one has graphite as bottom gate and other has Si as bottom gate.

Fig. S9 (a) and (c) shows the Landau fan diagram of R_{xx}/\square and R_{xy} respectively for sample 1.30° at $D=0V/nm$. We observe correlated insulators at $\nu=\pm 2, \pm 4$ only in this sample. Interestingly SC is observed only in electron side in this sample. Fig. S9 (b) and (d) shows the Landau Fan of R_{xx} and R_{xy} for sample with twist angle 1.50°, respectively at $D=0V/nm$. In this sample we observe Chern insulator states at $\nu=\pm 2, +3$ and ± 4 . A wide pocket of SC is observed on electron doping side in comparison to hole doping. No jumps in R_{xy} are observed in both samples around $B_z=0$.

Next, we analyzed the SC in both samples. Fig. S10 (a)-(c) shows the characterization of SC in sample with twist angle 1.30°. Fig. S10 (a) shows the temperature dependence (10mK to 1.2K) of dV/dI vs I_{dc} characteristics. The T_c of ~1.0 K is estimated from the R_{xx}/\square vs T plot, corresponding to the 90% drop in resistance, see Fig. S10 (b). The Ginzburg Landau equation, $B_{c2} = (\varphi_0/2\pi\xi_{GL}^2)(1 - \frac{T}{T_c})$, (where $\varphi_0 = h/2e$ is superconducting flux quantum, ξ_{GL} is coherence length) is fitted to the temperature dependence of B_{c2} taken at 90% drop in R_{xx} at that temperature, see fig. S10 (c). The upper critical field at 0K *i.e* $B_{c2}(0) \sim 0.13T$ is estimated from fitting which corresponds to $\xi_{GL} \sim 50nm$. Fig. S10 (d) shows the Fraunhofer pattern measured in e-S|N|h-SC configuration of 1.50° device.

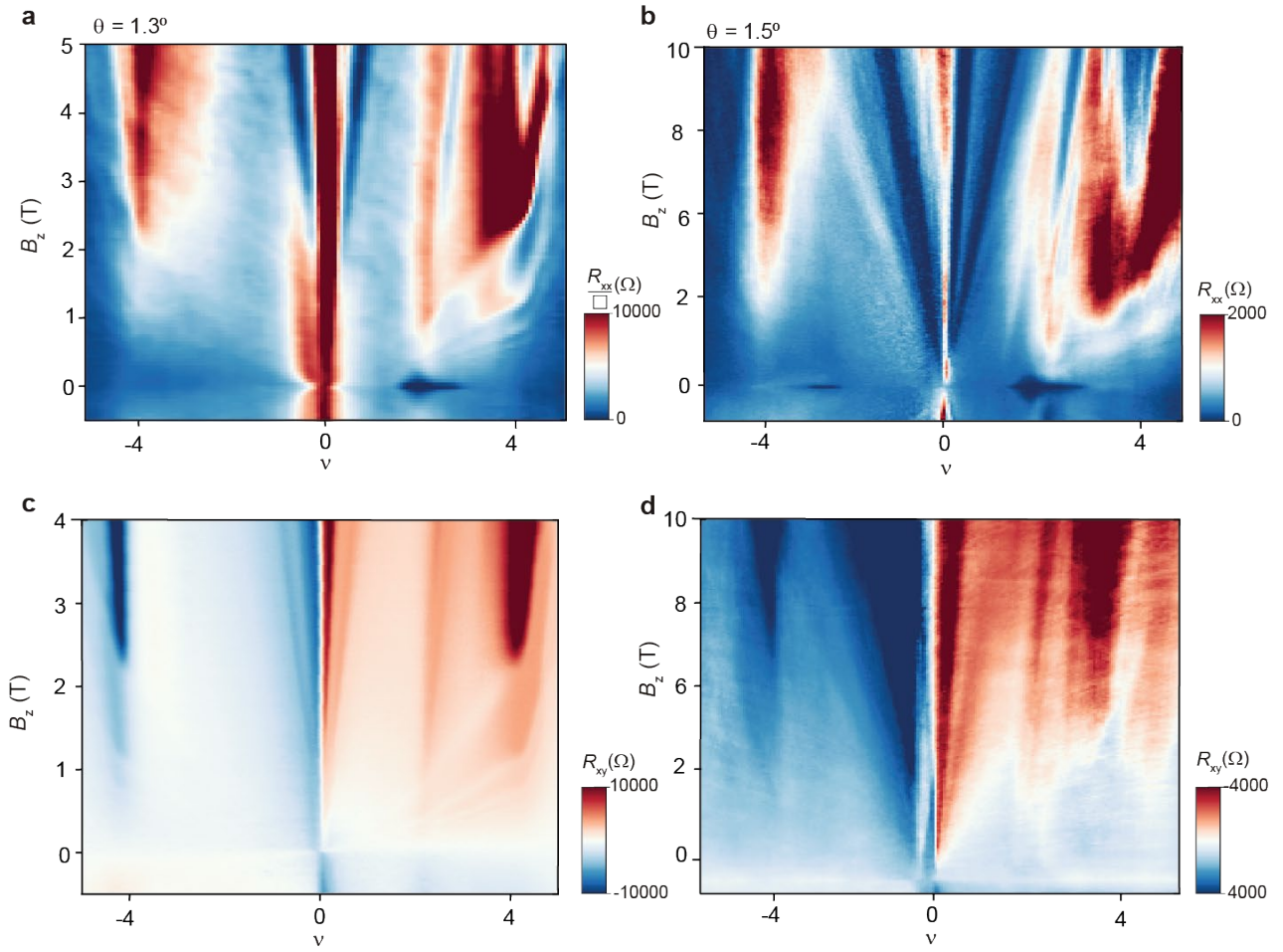


Figure S10: The Landau fan diagram (a) of R_{xx}/\square for TTG with twist angle 1.30° and (b) of R_{xx} for TTG with 1.50° measured at $D=0V/nm$ and 15mk. The Landau fan diagram of R_{xy} (c) for 1.30° TTG device at 300mK and (d) for 1.50° TTG device at 15mK and $D=0V/nm$.

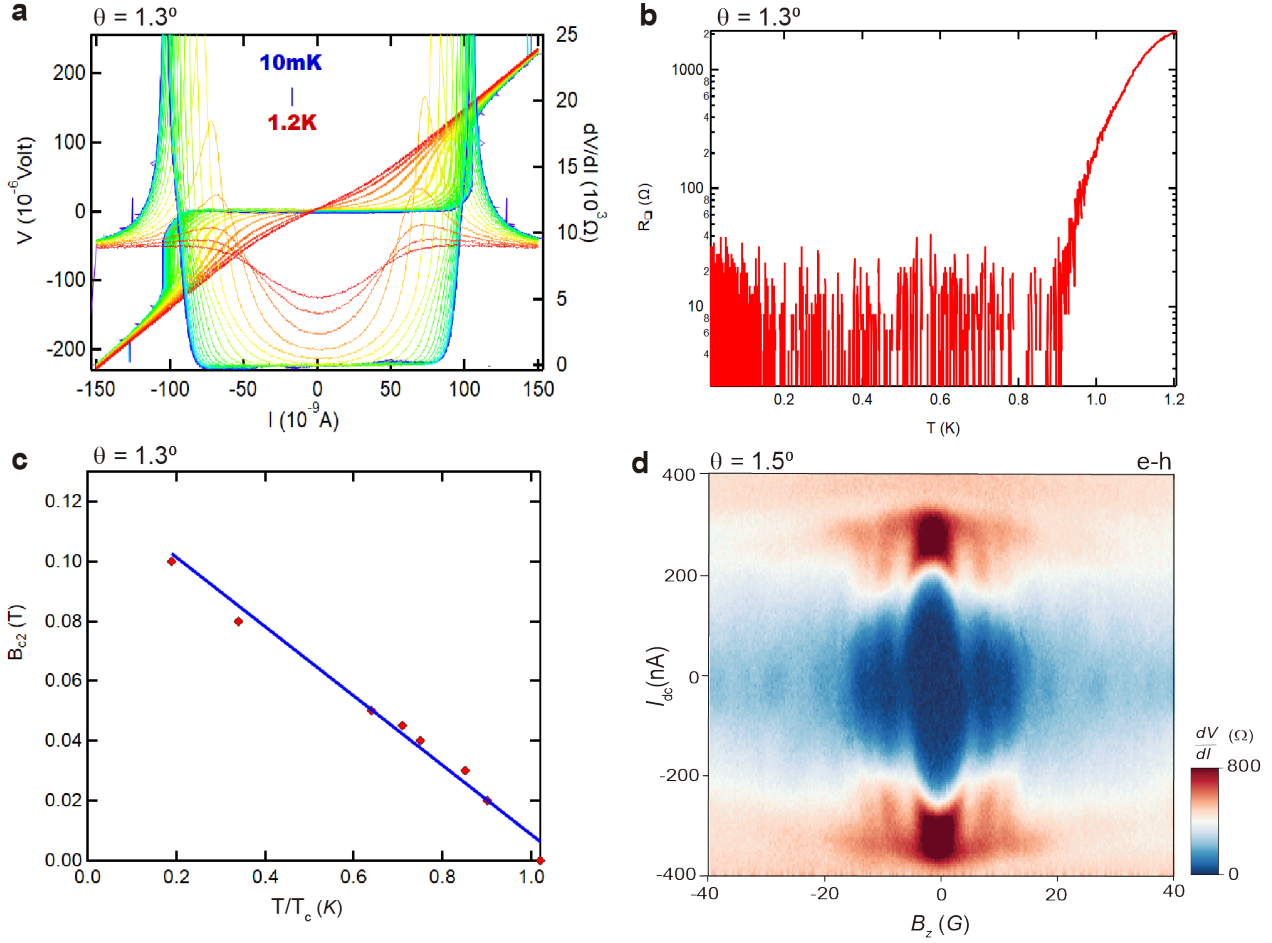


Figure S11: (a) IV characteristics of TTG device twist angle of 1.3° as the temperatures are varied from 10mK to 1.2K. (b) The R_{xx}/\square vs T curve for the same device with critical temperature $T_c=1$ K. (c) The critical magnetic field B_{c2} is plotted as a function of T/T_c and the $B_{c2}(0$ K) is estimated to be approximately 0.13 T. (d) Fraunhofer pattern of e-h doped superconducting pockets for the device with twist angle 1.5° .

References:

1. Bocarsly, M. *et al.* Imaging Coulomb interactions and migrating Dirac cones in twisted graphene by local quantum oscillations. *arXiv* (2024).
2. Shen, C. *et al.* Dirac spectroscopy of strongly correlated phases in twisted trilayer graphene. *Nat. Mater.* **22**, 316–321 (2023).
3. Zondiner, U. *et al.* Cascade of phase transitions and Dirac revivals in magic-angle graphene. *Nature* **582**, 203–208 (2020).
4. Hao, Z. *et al.* Electric field-tunable superconductivity in alternating-twist magic-angle trilayer graphene. *Science* **371**, 1133–1138 (2021).
5. Saito, Y. *et al.* Isospin Pomeranchuk effect in twisted bilayer graphene. *Nature* **592**, 220–224 (2021).

6. Xie, M. & MacDonald, A. H. Weak-Field Hall Resistivity and Spin-Valley Flavor Symmetry Breaking in Magic-Angle Twisted Bilayer Graphene. *Phys. Rev. Lett.* **127**, 196401 (2021).
7. Moshe, M., Kogan, V. G. & Mints, R. G. Edge-type Josephson junctions in narrow thin-film strips. *Phys Rev B* **78**, 020510 (2008).
8. Chen, S. *et al.* Current induced hidden states in Josephson junctions. *Nat. Commun.* **15**, 8059 (2024).
9. Fei, Z. *et al.* Two-dimensional itinerant ferromagnetism in atomically thin Fe₃GeTe₂. *Nat. Mater.* **17**, 778–782 (2018).
10. Li, Y. & Baberschke, K. Dimensional crossover in ultrathin Ni(111) films on W(110). *Phys. Rev. Lett.* **68**, 1208–1211 (1992).